

RESEARCH ARTICLE

10.1002/2014MS000417

Key Points:

- The proposed formulation is general enough to allow up or down-gradient CMT
- The net effect of the formulation is to produce large-scale circulation
- A novel superparameterized version of the WRF model is described and evaluated

Correspondence to:

S. N. Tulich,
stefan.tulich@noaa.gov

Citation:

Tulich, S. N. (2015), A strategy for representing the effects of convective momentum transport in multiscale models: Evaluation using a new superparameterized version of the Weather Research and Forecast model (SP-WRF), *J. Adv. Model. Earth Syst.*, 7, 938–962, doi:10.1002/2014MS000417.

Received 10 DEC 2014

Accepted 1 JUN 2015

Accepted article online 3 JUN 2015

Published online 30 JUN 2015

© 2015. The Authors.

This is an open access article under the terms of the Creative Commons Attribution-NonCommercial-NoDerivs License, which permits use and distribution in any medium, provided the original work is properly cited, the use is non-commercial and no modifications or adaptations are made.

A strategy for representing the effects of convective momentum transport in multiscale models: Evaluation using a new superparameterized version of the Weather Research and Forecast model (SP-WRF)

S. N. Tulich^{1,2}

¹CIRES, University of Colorado, Boulder, Colorado, USA, ²Physical Sciences Division, NOAA Earth System Research Laboratory, Boulder, Colorado, USA

Abstract This paper describes a general method for the treatment of convective momentum transport (CMT) in large-scale dynamical solvers that use a cyclic, two-dimensional (2-D) cloud-resolving model (CRM) as a “superparameterization” of convective-system-scale processes. The approach is similar in concept to traditional parameterizations of CMT, but with the distinction that both the scalar transport and diagnostic pressure gradient force are calculated using information provided by the 2-D CRM. No assumptions are therefore made concerning the role of convection-induced pressure gradient forces in producing up or down-gradient CMT. The proposed method is evaluated using a new superparameterized version of the Weather Research and Forecast model (SP-WRF) that is described herein for the first time. Results show that the net effect of the formulation is to modestly reduce the overall strength of the large-scale circulation, via “cumulus friction.” This statement holds true for idealized simulations of two types of mesoscale convective systems, a squall line, and a tropical cyclone, in addition to real-world global simulations of seasonal (1 June to 31 August) climate. In the case of the latter, inclusion of the formulation is found to improve the depiction of key synoptic modes of tropical wave variability, in addition to some aspects of the simulated time-mean climate. The choice of CRM orientation is also found to importantly affect the simulated time-mean climate, apparently due to changes in the explicit representation of wide-spread shallow convective regions.

1. Introduction

1.1. Superparameterization: Successes and Remaining Challenges

The difficult problem of convection parameterization needs no introduction. During much of the past 50 years, this problem could only be addressed through the use of relatively simple conceptual algorithms, embodying ideas about how convective cloud fields interact with their surroundings [e.g., *Arakawa and Schubert*, 1974]. With the recent advent of petascale computing systems, however, an alternative approach is now feasible, which involves embedding a series of relatively small, limited-area “cloud-resolving” models (CRMs) inside each grid box of a large-scale dynamical model; the embedded CRMs take the place of the large-scale model’s traditional convective and stratiform cloud schemes. This approach was first pioneered by *Grabowski and Smolarkiewicz* [1999] and *Grabowski* [2001], who proposed the name, “cloud-resolving convection parameterization.” Later, *Randall et al.* [2003] advocated the more provocative title, “superparameterization” (SP), to convey the fact that the embedded CRMs not only eliminate the need for conceptual models of deep convective cloud systems, but also conceptual models of the myriad of complex, spatially varying interactions among shallow and deep convection, radiation, aerosols, and the planetary boundary layer (PBL).

The SP approach has been implemented in several different global models, with a number of positive results being reported. For example, comparing their superparameterized formulation of the Community Atmosphere Model Version 3.0 (SP-CAM3) to its standard counterpart, *Khairoutdinov et al.* [2005] observed marked improvements in the simulated diurnal cycle of convection over land, as well as the simulated spectrum of convective-coupled tropical waves, including the intraseasonal Madden-Julian Oscillation (MJO), which was largely absent from the standard CAM3 [see also *Khairoutdinov et al.*, 2008; *Pritchard et al.*, 2011; *Randall et al.*, 2015]. Similar sorts of improvements were later reported by *Tao et al.* [2009], using a

completely different superparameterized global atmosphere model, known as the NASA Multiscale Modeling Framework (MMF). Meanwhile, in an extension of the SP approach to the coupled ocean-atmosphere Community Climate System Model Version 3.0 (SP-CCSM3), *Stan et al.* [2010] documented significant improvements in both the amplitude (reduced) and period (lengthened) of the simulated El Niño-Southern Oscillation. Such explicit-convection models are therefore attractive tools for addressing questions about the basic mechanisms underlying tropical weather and climate variability, as well as questions about how this variability might change in a warming world [e.g., *Grabowski*, 2003; *Thayer-Calder and Randall*, 2009; *Wyant et al.*, 2009; *Benedict and Randall*, 2011; *DeMott et al.*, 2011; *Andersen and Kuang*, 2011; *Arnold et al.*, 2013; *Pritchard and Bretherton*, 2014].

Despite its success, however, the SP approach is not without limitations. Perhaps most severe is that the embedded CRMs are typically configured to have two-dimensional (2-D) slab-symmetric geometry, for computational efficiency. This approximation, while apparently suitable for the coupling of thermodynamic (i.e., scalar) quantities, means that the CRM-simulated cloud fields can only interact directly with one component of the large-scale horizontal flow vector, namely that aligned parallel to the CRM domain [cf. *Randall et al.*, 2003]. Because the choice of CRM orientation is somewhat arbitrary, a common approach has been to simply neglect the tendency of the large-scale horizontal momentum due to CRM-scale convective transport processes. However, it appears that failing to include the effects of this unresolved *convective momentum transport* (CMT) can, in some cases, have a large negative impact on model performance [*Khairoutdinov et al.*, 2005; *Cheng and Xu*, 2014].

1.2. A Strategy for Advancing the 2-D SP Approach

In this paper, a general strategy for including the effects of CMT in 2-D SP models is proposed and evaluated. The idea is to emulate the standard approach taken in traditional mass-flux parameterizations of CMT (reviewed further in section 2; see also Figure 1a), where the problem is formulated as one of scalar transport in the presence of a diagnostic pressure gradient force. Rather than relying on a simple cloud model, however, here both the scalar transport and diagnostic pressure gradient force are calculated using the explicit CRM-simulated flow field. No assumptions are therefore made concerning the organization and transport properties of the underlying convection field, other than those implied through the use of a 2-D CRM. Because the transport and pressure gradient terms are both calculated using the embedded CRM, this strategy is referred to as “explicit scalar momentum transport” or ESMT.

The above strategy was devised as part of this study’s broader development of a new superparameterized version of the Weather Research and Forecast model (SP-WRF). Described herein for the first time, the SP-WRF is a versatile modeling framework that features all of the same capabilities as its standard counterpart, except grid nesting. The model can therefore be run in either global or regional configurations, using a variety of different physics options. Currently, these options include 6 different land surface packages, 7 different radiation packages, and 16 different microphysics packages (7 of which are double-moment). The option of continuous 3-D analysis nudging is also available, so that the model can be initialized gradually from a series of analyses, allowing spin-up of the embedded CRMs. These various capabilities stand in contrast to most other SP models, which were designed mainly for the purpose of simulating global climate. Moreover, while the development of previous SP models has typically involved stitching together models with different vertical grids and dynamical approximations, the SP-WRF has been formulated using a seamless single-model approach.

Section 2 provides an in-depth review of the methods and concepts behind traditional parameterizations of CMT. This review sets the stage for section 3, which describes the SP-WRF along with the proposed ESMT formulation. Section 4 discusses the effects of including this formulation in idealized simulations of two types of mesoscale convective systems (MCSs): a squall line and a tropical cyclone. This evaluation is extended to real-world applications in section 5, which describes a series of seasonal climate integrations. Section 6 provides a summary and discussion of the main findings.

2. Review of Traditional Methods for Parameterizing CMT

The process of CMT is among the dominant contributors to the apparent momentum source \mathbf{X} in the free troposphere [*Tung and Yanai*, 2002]; gravity wave transports also provide an important but generally

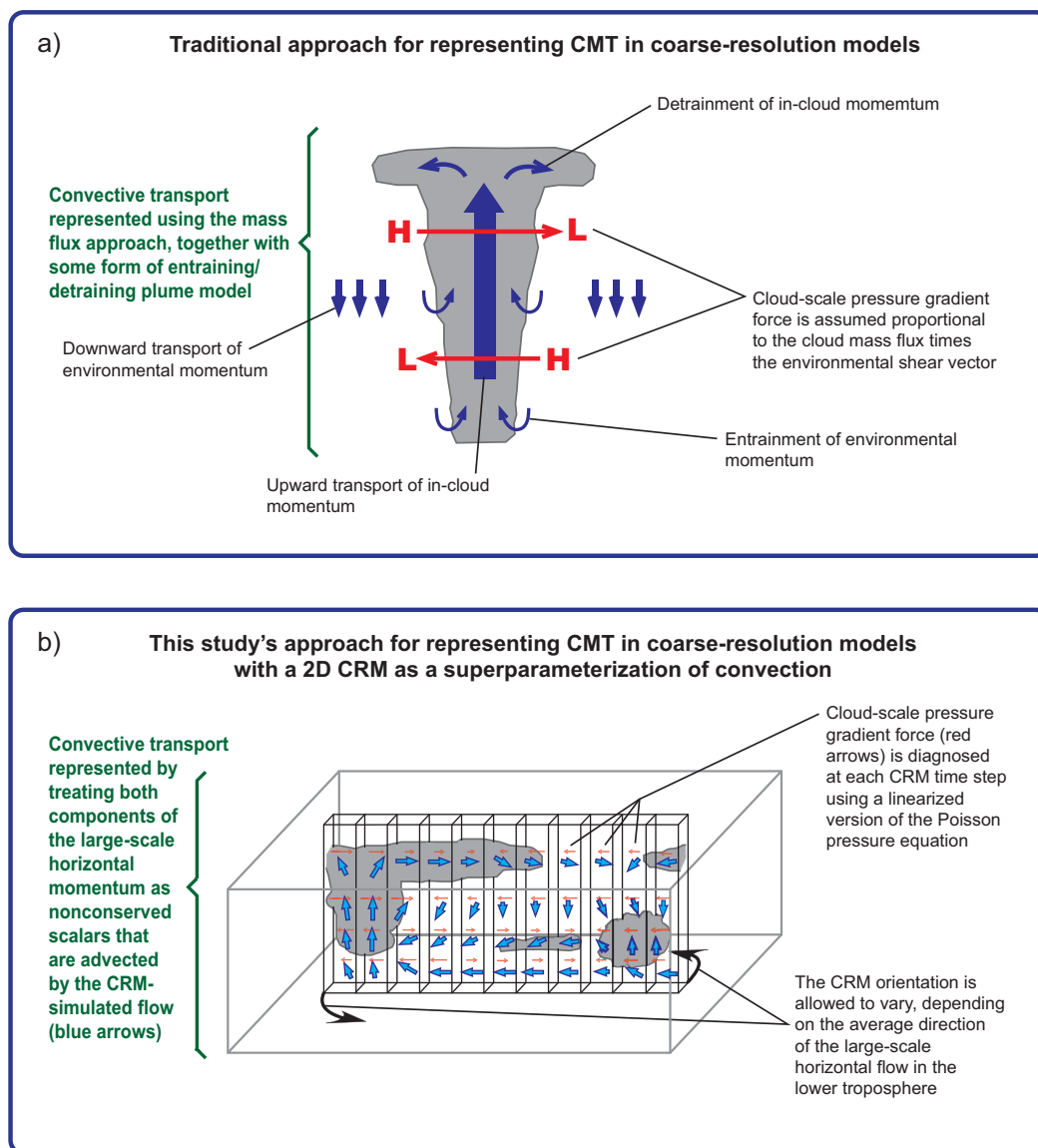


Figure 1. Schematic comparison of (a) the traditional approach for representing CMT in coarse-resolution models versus (b) the approach proposed here for 2-D SP models.

secondary contribution [Lane and Moncrieff, 2010; Shaw and Lane, 2013]. Traditional parameterizations of CMT have almost universally been formulated using the mass-flux approach [e.g., Schneider and Lindzen, 1976; Shapiro and Stevens, 1980; Zhang and Cho, 1991; Wu and Yanai, 1994; Gregory et al., 1997]. The idea is to partition the vertical motion field into regions of upward and downward motion, where the former are assumed to be cloudy and occupy only a small fraction of the domain, while the latter are assumed to be cloud-free and occupy the remaining part of the domain, called the “environment.” In the absence of source/sink terms, the problem is then one of determining the cloud base mass flux together with the fractional entrainment and detraining rates as a function of height. Physically, momentum is transported upward from low levels and deposited aloft by convective updrafts, while momentum in the surrounding environment is transported downward by compensating subsidence (see the schematic in Figure 1a). The net effect of this parameterized CMT is to produce large-scale “cumulus friction” [Schneider and Lindzen, 1976].

In reality, however, convection also introduces horizontal pressure gradient forces that can strongly affect the upscale forcing of momentum [Rotunno and Klemp, 1982; LeMone et al., 1984; Soong and Tao, 1984;

Lemone et al., 1988; Lafore et al., 1988]. Studies aimed at parameterizing these effects have typically started off with a linearized, anelastic version of the Poisson pressure equation, expressed here as:

$$-\nabla^2\pi = 2\nabla_{\mathbf{H}}w \cdot \frac{\partial\mathbf{U}_{\mathbf{H}}}{\partial z}, \quad (1)$$

where π is the perturbation pressure divided by the basic state density, $\nabla_{\mathbf{H}}$ is the horizontal vector derivative, w is the perturbation vertical velocity, and $\mathbf{U}_{\mathbf{H}}$ is the basic state horizontal wind vector. Assuming sinusoidal variations of the cloud updraft region, this equation can then be used to derive an expression for the updraft-averaged horizontal pressure gradient force:

$$\mathbf{F} = \left(\alpha_x M \frac{\partial \bar{U}}{\partial z}, \alpha_y M \frac{\partial \bar{V}}{\partial z} \right), \quad (2)$$

where M is the cloud mass flux and $\alpha \equiv (\alpha_x, \alpha_y)$ is a dimensionless vector whose components are both greater than zero and depend solely on the spatial organization of the flow. This expression was first obtained by Wu and Yanai [1994], hereafter WY94, who treated \mathbf{F} as a source/sink term in the mass-flux equation expressing conservation of cloud momentum [see also Gregory et al., 1997]. Closure of the problem then requires an appropriate choice of α .

To provide an upper bound on the magnitude of α , WY94 considered two limiting cases of convective organization: quasircular versus quasilinear. In the first case, called “unorganized,” α_x and α_y are roughly equal and have values less than unity, i.e., $0 < \alpha_x \approx \alpha_y < 1$. The net effect of the source/sink term \mathbf{F} in this case is to reduce the cloud mass flux by a factor $1 - \alpha$, where $\alpha \equiv |\alpha|$ [see also Romps, 2012]. In the second case, called “organized,” α is oriented roughly perpendicular to the convective line and has magnitude always less than two, i.e., $0 < \alpha < 2$. In the special situation when $\alpha > 1$, the net effect of \mathbf{F} is to provide *up-gradient* CMT (i.e., accelerate the large-scale flow) in the direction perpendicular to the convective line.

Although there is clear evidence in nature of storms with $\alpha > 1$ [e.g., Lemone et al., 1988], it has become standard practice among model developers to assume convection is always unorganized with fixed $\alpha < 1$ [e.g., Pope et al., 2000; Mizuta et al., 2006; Kim et al., 2008; Richter and Rasch, 2008]. This assumption has been guided mainly by the work of Zhang and Wu [2003], who looked carefully at a multiweek 2-D-CRM simulation of convection with realistic large-scale forcing. Using linear regression techniques, they inferred typical values of α in the range 0.5–0.6, slightly smaller than the value of 0.7 suggested by Gregory et al. [1997] on the basis of shorter-term 3-D calculations. The implication is that, on average, even 2-D convection tends to produce down-gradient CMT, contrary to what might naively be expected [see also Mapes and Wu, 2001].

In summary, the standard treatment of CMT is essentially that of scalar transport in the presence of a diagnostic source/sink term. The transport is handled using the mass-flux approach, while the source/sink term is diagnosed using the Poisson pressure equation (1). Assumptions needed to close this treatment include those surrounding the representation of cloud entrainment and detrainment (through the choice of a particular cloud model), as well as those surrounding the representation of cloud organization (through the choice of α). The key to arriving at the ESMT formulation proposed here (detailed in section 3.3; see also the sketch in Figure 1b) is to recognize that most of these assumptions/choices are unnecessary when using a 2-D CRM as a parameterization for convection.

3. Model Description

The SP-WRF is a multiscale modeling framework based on Version 3.4.1 of the Advanced-Research WRF system (ARW). A detailed description of the ARW can be found in Skamarock et al. [2008], so only a brief overview is given below.

3.1. Overview of the ARW

The ARW is a fully compressible, nonhydrostatic model with a terrain-following hydrostatic-pressure vertical coordinate, defined as $\eta \equiv (p_h - p_{ht})/\mu$, where p_h is the hydrostatic component of pressure (excluding moisture), p_{ht} is the value of p_h along the model top, and μ is the total-column dry air mass per unit area. The

latter is defined as $\mu \equiv p_{hs} - p_{ht}$, where p_{hs} is the value of p_h along the surface, so that η varies between 1 at the surface and 0 at the model top.

The governing equations are expressed in flux form using finite difference approximations. Time differencing is handled using the split-explicit integration scheme of *Wicker and Skamarock* [2002]. The scheme is third-order accurate for the nonacoustic modes and is designed to ensure conservation of mass and other single-moment flux quantities [*Klemp et al.*, 2007]. The spatial stencils for advection are fifth-order accurate in the horizontal direction and third-order accurate in the vertical. To prevent the development of negative mixing ratios, the advection of water substance is generally handled using the positive-definite flux renormalization technique of *Skamarock and Weisman* [2009]. The one exception is in the case of spherical geometry, where the flux renormalization is applied everywhere but at the northern and southern polar boundaries—any negative mixing ratios that develop at these locations are automatically set to zero. This approach for handling the positive-definite transport of water on the sphere is not available in the standard ARW, but rather was added as part of this study, through consultation with the WRF development team at NCAR (*W. Skamarock*, personal communication, 2011).

3.2. Coupling Method for Scalars

In the SP-WRF, the ARW serves as both the large-scale model (LSM) and its embedded 2-D CRMs. These two components are coupled through exchanges of heat, moisture, and momentum tendencies. The tendencies passed from the LSM to the CRM are referred to as the large-scale “forcing,” while those passed from the CRM to the LSM are referred to as the small-scale “feedback.” Below is a general description of the algorithm used to calculate these two sets of tendencies, given in the context of a generic scalar variable q . To simplify the discussion, the effects of changes in the total-column dry air mass μ are not considered. The algorithm is identical to that used in the SP-CAM3 (reviewed in *Randall et al.* [2015]), except that no adjustment of the CRM vertical grid is needed during the course of the model integration, since the CRM and LSM vertical grids are the same.

The large-scale forcing is obtained by advancing the LSM from time level n to $n + 1$ to generate a *provisional* value of q that depends only on the large-scale processes of advection and horizontal diffusion. Conceptually, we can write:

$$\widetilde{q}_L^{n+1} = q_L^n + \Delta t_L (A_L + H_L), \tag{3}$$

where the subscript L denotes an LSM value, the quantity Δt_L is the LSM time step, and the terms A_L and H_L represent the LSM-computed tendencies of q_L due to resolved advection and parameterized horizontal diffusion, respectively. The large-scale forcing of the CRM variable q_c is then defined as:

$$LSF_q \equiv \frac{\widetilde{q}_L^{n+1} - \langle q_c^n \rangle}{\Delta t_L}, \tag{4}$$

where the quantity $\langle q_c^n \rangle$ represents the horizontal CRM average of q_c at the start of the LSM time step.

The forcing in (4) is applied to the CRM during its integration between time levels n and $n + 1$. The predictive equation for q_c can then be written as:

$$\frac{q_c^{m+1} - q_c^m}{\Delta t_c} = S_c + V_c + H_c + A_c + LSF_q, \tag{5}$$

where the superscripts m and $m + 1$ denote successive time steps of the CRM, the quantity Δt_c is the CRM time step (which is an integer division of Δt_L), and the terms S_c and V_c represent the CRM-calculated tendencies of q_c due to diabatic processes and parameterized turbulent vertical diffusion, respectively. This equation is solved for each of the embedded CRMs, assuming periodic horizontal boundary conditions.

The small-scale feedback is obtained by overwriting the provisional LSM value of q at time level $n + 1$ with the horizontal average of the CRM value, i.e., $q_L^{n+1} = \langle q_c^{n+1} \rangle$. The predictive equation for q_L can thus be written as:

$$\frac{q_L^{n+1} - q_L^n}{\Delta t_L} = A_L + H_L + SSF_q, \tag{6}$$

where the last term on the right hand side is the small-scale feedback, defined as:

$$SSF_q \equiv \frac{\langle q_c^{n+1} \rangle - \widetilde{q}_L^{n+1}}{\Delta t_L}. \quad (7)$$

The coupling of scalars between the LSM and CRM is therefore formulated as a kind of mutual relaxation of the large and small-scales toward one another on a relaxation time scale Δt_L . Unlike traditional relaxation methods, however, the relaxation of the small to large scales is held constant during the integration of the CRM from time levels n to $n + 1$.

3.3. Formulation of Explicit Scalar Momentum Transport (ESMT)

The method used to couple the large and small-scale momentum components is somewhat different from that outlined above for scalars. Letting u_c denote the horizontal wind variable of the 2-D CRM, the large-scale forcing of u_c is defined as:

$$LSF_u \equiv \frac{\widetilde{u}_L^{n+1} \cos(\beta) + \widetilde{v}_L^{n+1} \sin(\beta) - \langle u_c^n \rangle}{\Delta t_L}, \quad (8)$$

where u_L and v_L are the east-west and north-south components of the LSM wind vector, respectively, while the variable β denotes the orientation angle of the CRM domain within the LSM grid box (see Figure 1b). Following the suggestion of Grabowski [2004], the angle β is chosen to match that of the mean large-scale wind vector in the lowest 4 km. The rationale is that most fast-moving squall-line systems (which essentially behave like quasi-2-D convection) are often seen to be oriented perpendicular to the low-level vertical shear vector [Barnes and Sieckman, 1984; LeMone et al., 1998; Tulich and Kiladis, 2012]. Of course, such shear-perpendicular lines are just one of several different “modes” of linear convective organization, including shear-parallel cloud “streets” [Young et al., 2002]. Thus, this approach could likely be improved upon. Further discussion of this issue is left until section 5.3.

The small-scale feedback is obtained by treating the large-scale wind components u_L and v_L as nonconserved scalars that are advected and diffused by the CRM-simulated flow field. The corresponding scalar wind variables are denoted by \hat{u}_c and \hat{v}_c , respectively, where the prediction of each is obtained using (5), but with S_c now representing the source/sink due to convection-induced horizontal pressure gradient forces. As in the conventional mass-flux formulation of WY94, the pressure source/sink is approximated using the linearized, anelastic version of the Poisson pressure equation (1). In the context of the 2-D CRM, this equation can be written generically as:

$$-\frac{\partial^2 \hat{\pi}_c}{\partial \chi^2} - \frac{\partial^2 \hat{\pi}_c}{\partial z^2} = 2 \frac{\partial w_c}{\partial \chi} \frac{\partial \langle q_c \rangle}{\partial z}, \quad (9)$$

where χ denotes horizontal position in the CRM and q_c now represents either of the scalar wind variables (\hat{u}_c or \hat{v}_c). The implicit assumption is that the spatial structure of the advecting flow field is the same in both horizontal directions of the LSM, for lack of additional information (i.e., the 2-D CRM cannot account for the 3-D structure of the underlying flow field). Taking the horizontal derivative of (9) and defining $S_c \equiv -\partial \hat{\pi}_c / \partial \chi$ leads to the diagnostic equation:

$$\frac{\partial^2 S_c}{\partial \chi^2} + \frac{\partial^2 S_c}{\partial z^2} = 2 \frac{\partial^2 w_c}{\partial \chi^2} \frac{\partial \langle q_c \rangle}{\partial z}. \quad (10)$$

Solutions to this equation are obtained at each CRM time step using Fourier transform methods in the horizontal direction together with a tridiagonal matrix solver in the vertical direction. The small-scale feedback is then obtained using (7), evaluated for each of the large-scale wind components. The total computational cost of the feedback algorithm is typically around 10% of the model execution time.

To help interpret the impacts of the above formulation, it is useful to note that (10) can be solved analytically in certain idealized situations. For example, in the case of an isolated cloud updraft with sinusoidal variations, WY94 showed that:

$$S_c = \alpha_c \left[w_c \frac{\partial \langle q_c \rangle}{\partial z} \right], \quad (11)$$

where the interpretation and physical significance of α_c has already been discussed. In the SP-WRF, an empirical estimate of α_c is obtained during each CRM time step of the model integration, by horizontally regressing the quantity in square brackets on the right hand side of (11) against the diagnostic pressure source/sink S_c . This analysis is performed at each level in the vertical and for both horizontal directions of the LSM, so that the resulting regression coefficients, denoted α_x and α_y , are functions of both large-scale space and time.

A distinctive feature of the proposed ESMT formulation is that both components of the momentum feedback are handled using the exact same formalism, despite the reliance on a 2-D CRM with variable orientation. This parity is achieved by carrying two scalar wind variables in the model, one for each horizontal direction. In principle, however, there is no practical reason why an alternative formulation could not be devised, in which only a single scalar wind variable is carried by the model, to account for the feedback in the direction perpendicular to the 2-D CRM domain—the component in the direction parallel could then be obtained through the fully nonlinear calculation of CMT that is automatically performed by the CRM as parts of its normal integration, i.e., the CMT associated with the horizontal wind variable u_c . This hypothetical alternative (which is 50% cheaper than the original, but at the expense of parity) is similar to what was proposed early on by *Grabowski* [2004]. The only difference is that here an attempt is made to account for the effects of convection-induced pressure gradient forces in directions unaccounted for by the 2-D CRM, i.e., the scalar wind variable is generally treated as a nonconserved (rather than conserved) quantity. The rationale is that convection in the real world is invariably a 3-D phenomenon, so the effects of pressure variations must generally be considered in both horizontal directions.

In agreement with this last point, *Cheng and Xu* [2014] recently proposed a much simpler strategy for representing the effects of CMT in the CRM-perpendicular direction of 2-D SP models. Briefly, their idea is to adopt the standard mass-flux approach with fixed $\alpha=0.4$, but where the convective mass flux is taken directly from the CRM-simulated vertical velocity field w_c . No assumptions are therefore made concerning the rates of convective entrainment and detrainment. While computationally less expensive than the approach devised here, a potential drawback to their mass-flux-style formulation is that no allowance is made for large-scale variations in α . Evidence of these variations can be found later in Figure 6b.

3.4. Treatment of Unresolved Physical Processes

As already mentioned, the SP-WRF features a variety of different options for the treatment of physical processes that are unresolved by the CRM, such as microphysics and radiation. Here, however, the description is given in the context of a single set of physics packages that can serve as a baseline for future sensitivity studies. Specifically, the microphysics package is the single-moment scheme of *Tao et al.* [2003], with five hydrometeor categories: cloud water, cloud ice, rain, snow, and graupel. The radiation package is a broadband formulation with 10 bands in the thermal part of the spectrum and 11 bands in the solar [*Chou and Suarez*, 1999; *Chou et al.*, 2001]. For computational efficiency, calls to the radiation are performed every 20 min of simulation time on the CRM grid. The cloud fraction is assumed to be zero or one, depending on a cloud condensate threshold of 10^{-6} g kg⁻¹.

The effects of unresolved turbulent mixing in the CRM are parameterized using a 1.5 order turbulence kinetic energy (TKE) scheme. Although originally developed for use in large-eddy simulation models by *Deardorff* [1980], this type of scheme has since been implemented in a number of CRMs, including those utilized in both the SP-CAM3 and NASA MMF. The scheme adopted here is similar to that of *Skamarock et al.* [2008].

In the case of the LSM component of the SP-WRF, only horizontal mixing is parameterized for scalars, using a variation of the ARW's standard 2-D Smagorinsky scheme. This scheme is also used for momentum, but with the additional effects of orographic gravity wave drag parameterized using an algorithm that accounts for wave breaking in both the lower troposphere and lower stratosphere, following *Kim and Arakawa* [1995] and *Hong et al.* [2006]. To minimize the unwanted effects of gravity waves reflecting off of the upper boundary, damping of the vertical velocity is applied in the uppermost levels of both the CRM and LSM, using the implicit damping scheme of *Klemp et al.* [2008].

Processes involving interactions between the atmosphere and surface are handled somewhat differently, depending on whether the embedded CRMs are situated over water or land. Over water, the surface fluxes

of heat, moisture, and momentum are parameterized using the COARE algorithm of *Fairall et al.* [2003]; meanwhile, the prognostic scheme of *Zeng and Beljaars* [2005] is used in each of the CRM grid columns to account for the diurnal evolution of the sea surface skin temperature. Based on Monin-Obukhov similarity theory, the COARE algorithm is a bulk flux scheme that features empirically derived formulations for the velocity and scalar roughness lengths. The stability-dependent profile functions are a blend of semiempirical and theoretical forms that are free of singularities over a broad range of stability conditions. The COARE algorithm is currently not available in the standard ARW, but rather was added as part of this study to place the model on a firmer observational footing.

For model points over land, the COARE algorithm is still used to compute the surface fluxes, but with a different set of expressions for the velocity and scalar roughness lengths. The velocity roughness length is specified on the basis of vegetation type, while the thermal and moisture roughness lengths are specified using the analytical form proposed by *Zilitinkevich* [1995]. To predict the evolution of the land surface/hydrology, the comprehensive Noah model of *Chen and Dudhia* [2001] is applied in each of the CRM grid columns. This approach of handling all surface-related processes on the CRM grid is unique in comparison to most other SP formulations, which instead handle these processes on the LSM grid, for ease of implementation. It is left as a question for future research as to whether this small versus large-scale treatment of surface processes has any systematic influence on the model's performance.

3.5. Parallel Computing Performance

The SP-WRF is designed to run on massively parallel computing systems that can potentially yield a significant speedup over single-processor calculations. To estimate the amount of speedup that is achieved in practice, a series of 6 day global integrations was performed using the NOAA's CRAY XE6 (Gaea) computing platform. The model configuration is very similar to that described later in section 5. As shown in Figure 2a, the amount of speedup is essentially at its theoretical limit for processor counts N_p in the range 128–2048. For larger processor counts, however, the model becomes increasingly less efficient as N_p approaches the hard limit, $N_p = N_L$, where N_L is the total number of LSM grid columns (8192 in the current example). This efficiency loss, which peaks at a modest value of around 20%, is due to increased latency of message passing as the LSM becomes distributed over larger processor counts. For the case with $N_p = 1024$, Figure 2b shows that the typical throughput is 1 simulated day per 14.5 min of wall-clock time.

4. Idealized Simulations of Two Types of MCSs

As a first step in evaluating the SP-WRF, this section describes a series of idealized simulations of two types of mesoscale convective phenomena: a squall line and a tropical cyclone. A primary goal is to see how adopting the proposed ESMT formulation affects the simulated storm morphology. To this end, an alternative formulation of the momentum feedback is also considered that consists of neglecting both the advective and source terms in (5) so that the feedback involves only the processes of turbulent diffusion and surface friction. This diffusion-only formulation is defined here as the "control," since it is essentially what is adopted in most other SP models, including the SP-CAM3, SP-CCSM3, and NASA MMF.

4.1. Squall Line Case

The experimental setup for the squall line case is as follows. The LSM is configured as a nonrotating, doubly periodic box with 16×16 columns at 32 km horizontal grid spacing. The embedded CRMs each have 16 columns at 2 km horizontal grid spacing. The vertical grid has 65 levels with spacing stretching from roughly 50 m near the surface to around 500 m at and above 5 km. The model top is at roughly 28 km with gravity wave damping applied in the uppermost 7 km. The large and small-scale time steps are 2 min and 10 s, respectively. The lower boundary is a uniform ocean with skin temperature held fixed at 301 K. Convection is maintained through imposed advective cooling and moistening tendencies, applied uniformly on the LSM grid. The generic expression for these tendencies is given by $-W\partial\langle q_L \rangle/\partial z$, where W is a specified tropospheric vertical motion profile with top-heavy structure as shown in Figure 3a. For simplicity, the effects of radiation are handled using the idealized treatment of *Pauluis and Garner* [2006], as opposed to the standard radiation scheme described earlier in section 3. To ensure an environment that is favorable for squall line formation, nudging is applied to the domain-averaged horizontal wind components of the LSM with a 1 h nudging time scale. The target wind profile is a sheared low-level easterly jet, as shown in Figure

SP-WRF parallel computing performance

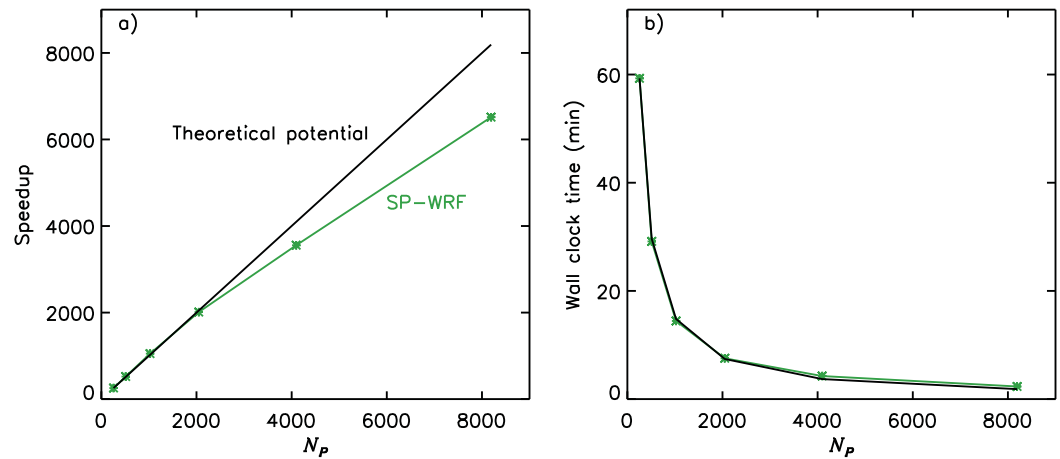


Figure 2. Parallel computing performance of the SP-WRF on the NOAA’s CRAY XE6 (Gaea) computing platform. (a) Speedup and (b) measured wall-clock time per simulated day plotted as a function of the number of computing processors (N_p). Green symbols denote the actual model timing, while the black line denotes the theoretical potential under linear scaling. Results are based on the last 5 days of a 6 day global simulation, with no output to disk. The grid spacing of the LSM is roughly $2.8^\circ \times 2.8^\circ$; the embedded CRMs each have 32 columns at 4 km grid spacing. The vertical grid has 51 levels. The large and small-scale time steps are 10 min and 20 s, respectively.

3b, which is broadly representative of the climatological easterly jet over northern west Africa during summer, where westward-moving squall lines are common [Rickenbach *et al.*, 2009; Cetrone and Houze, 2011; Tulich and Kiladis, 2012]. The initial large-scale temperature and moisture profiles are representative of conditions observed over the tropical north Atlantic during the GATE field campaign. Convection is initiated in the model by introducing a low-level temperature perturbation to the LSM grid that is slab symmetric in the north-south direction with a horizontal scale in the east-west direction of 128 km. To break the initial symmetry in the north-south direction, random small-amplitude ($<0.1K$) perturbations are added to the large-scale temperature field near the surface.

The model is evaluated against a 3-D CRM benchmark calculation, performed using the stand-alone ARW with 2 km horizontal grid spacing and the same forcing as described above. To make the comparison as fair as possible, output from the 2 km ARW is spatially coarse-grained to have the same 32 km horizontal grid spacing as the SP-WRF. This sort of benchmark evaluation has become common in

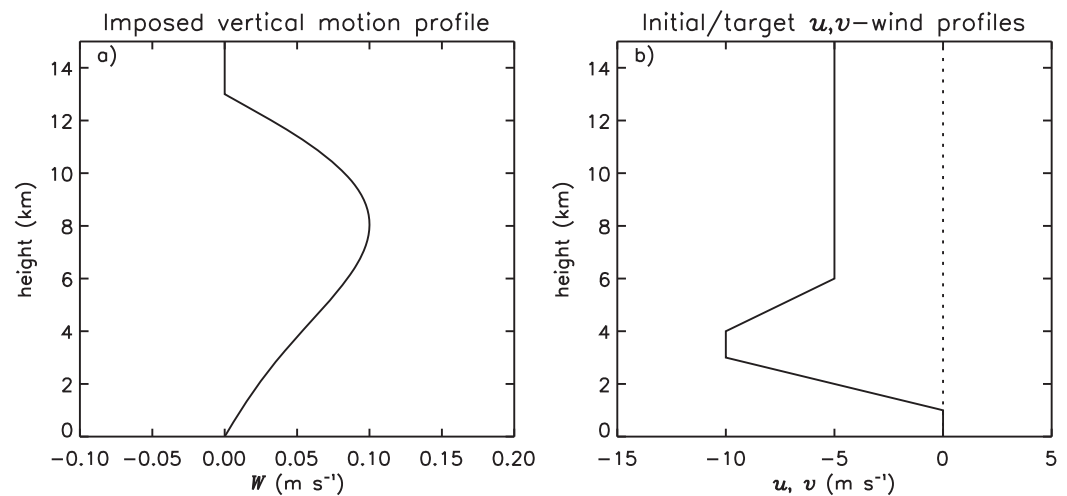


Figure 3. Profiles of the (a) large-scale vertical motion and (b) initial/target background u and v -wind profiles (solid and dotted, respectively) imposed in the idealized squall line experiment.

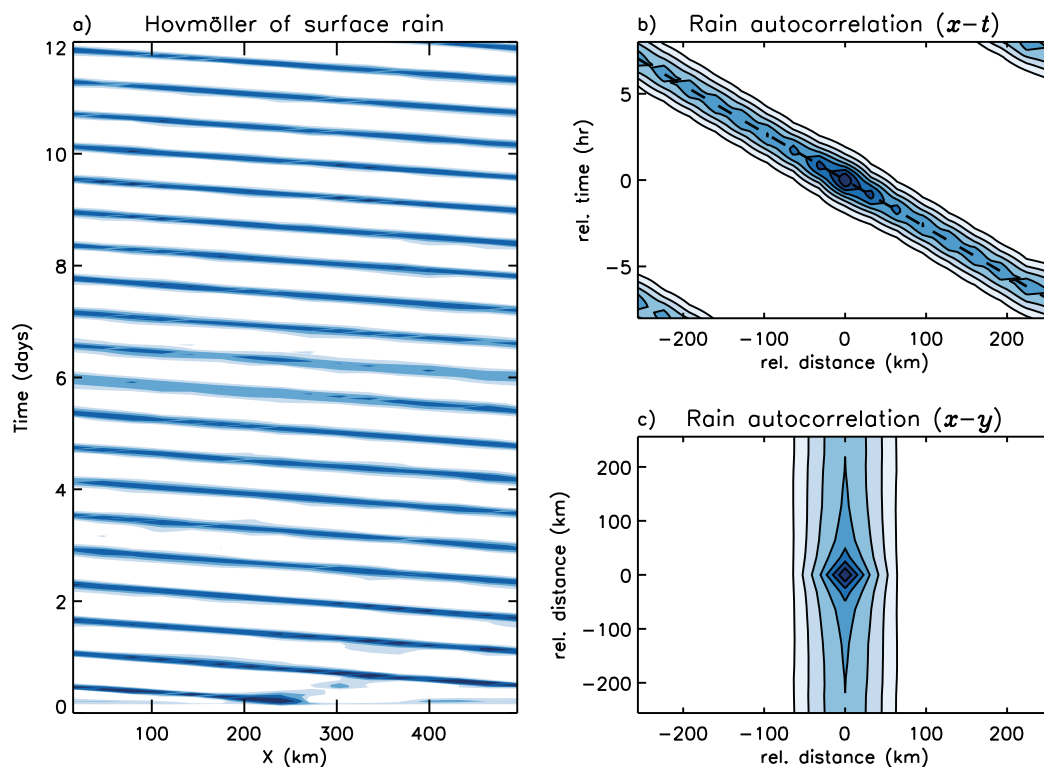


Figure 4. Simulated rain evolution and horizontal structure of the idealized squall-line produced in the benchmark 3-D CRM. (a) Hovmöller of surface rain averaged in the y direction. (b) Lagged autocorrelation of y -averaged surface rain as function of horizontal distance (x direction) and time; the dashed line denotes a phase speed of 9.8 m s^{-1} . (c) Time average of the spatial autocorrelation of rain. Contours in Figures 4b and 4c start at 0.3 with intervals of 0.1.

multiscale modeling studies where the large and small-scale components of the multiscale model are the same [e.g., Jung and Arakawa, 2005; Grabowski, 2006; Jung and Arakawa, 2014; Slawinska et al., 2015].

As shown in Figure 4, the benchmark features a long-lived squall line system that moves westward at a well-defined speed of 9.8 m s^{-1} , just slightly slower than the imposed easterly jet maximum of 10 m s^{-1} between $z = 3$ and 4 km (see Figure 3b). The zonal scale of the disturbance in terms of rainfall is roughly 100 km , much larger than the $O(1 \text{ km})$ scale of a typical deep convective updraft. The composite longitude-height structure of the disturbance in Figure 5a shows the familiar pattern in cloudiness of a leading convective line and trailing stratiform anvil region. The associated temperature and moisture signals imply strong convective destabilization at low-levels toward the leading half of the cloud line, in the form of a “wedge” of anomalously cool and moist air situated just above the PBL between $z \approx 1$ and 2.5 km . Convection is strongest when virtual temperature T_v anomalies near the top of the convective inhibition layer at $z \approx 3.5 \text{ km}$ [cf. Tulich and Mapes, 2010] switch from positive to negative, implying removal of a “capping” inversion. The system’s surface-based cold pool extends well behind the cloud line and features a maximum temperature depression of roughly 0.9 K . The latter is located more than 30 km to the rear of the heaviest surface rainfall, suggesting that the system is propagating faster than the surface-based cold pool. Overall, the structures and implied dynamics of the disturbance are very similar to those obtained previously by Tulich and Kiladis [2012] in the context of observed west African squall lines (see their Figure 11).

The SP-WRF is able to capture most of the above storm features, regardless of the small-scale momentum feedback, as illustrated in Figures 5b and 5c. The main deficiencies are that the SP-simulated cloud lines move slightly slower (9.0 m s^{-1}) than in the benchmark case and are generally too strong in dynamic intensity at low levels, especially near the surface and toward the top of the convective inhibition layer. The latter problem is mitigated to some extent in the run with ESMT (Figure 5c), suggesting

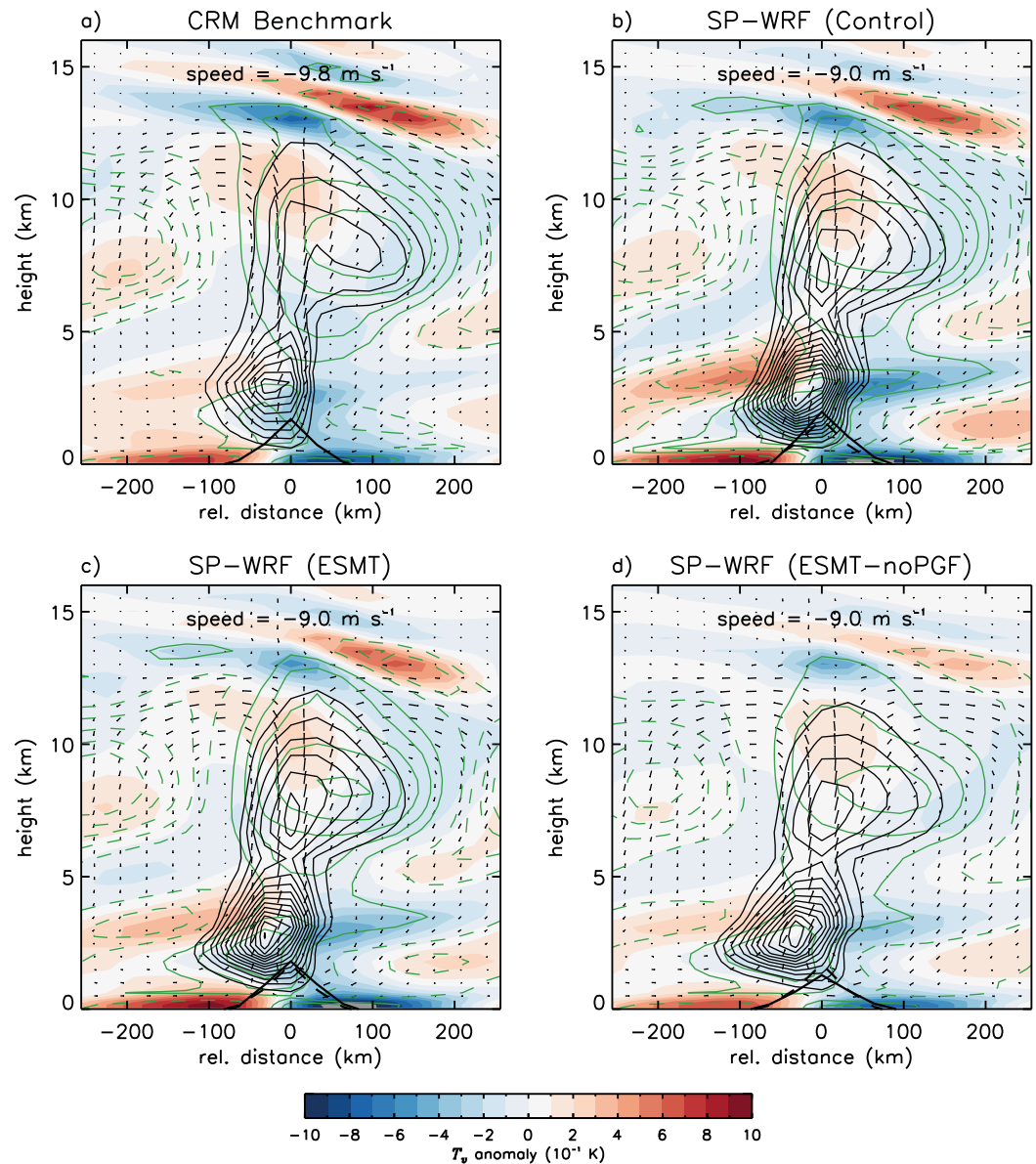


Figure 5. Composite longitude-height (x - z) structures of the simulated squall line in the (a) CRM benchmark versus the (b) control, (c) ESMT, and (d) noPGF versions of the SP-WRF. All fields are plotted as anomalies with respect to the horizontal domain average. Shading denotes the virtual temperature, while thin black contours denote the cloud water/ice mixing ratios with intervals of 0.2 g kg^{-1} (only positive values shown). Green contours denote the relative humidity with intervals of $\pm 2\%$ (negative values are dashed). Arrows denote wind vectors in the x - z plane. The heavy solid line at the bottom of each plot denotes the composite surface rainfall (only positive values shown), with the same arbitrary units throughout. For ease of comparison, the composite surface rainfall from the CRM benchmark in Figure 5a is denoted by the heavy dashed line in Figures 5b–5d.

that the net effect of the explicit momentum feedback is to weaken the disturbance, via cumulus friction.

To assess the role of the parameterized horizontal pressure gradient force, an additional run was performed with the scalar momentum source/sink term S_c in (5) set to zero, referred to as run noPGF. Figure 5d shows that the disturbance in this case is even weaker than before, with a roughly 20% smaller maximum in surface rainfall than in the benchmark case. The implication is that the parameterized pressure gradient force is acting to offset a portion of the explicit cumulus friction, much like in traditional parameterizations of CMT with $0 < \alpha < 1$. The latter interpretation is further supported by Figure 6, which shows that regression-derived values of α_x and α_y are both typically in the range 0–1. A notable exception is near the surface, where values are often well outside this range, apparently due to the effects of the lower boundary.

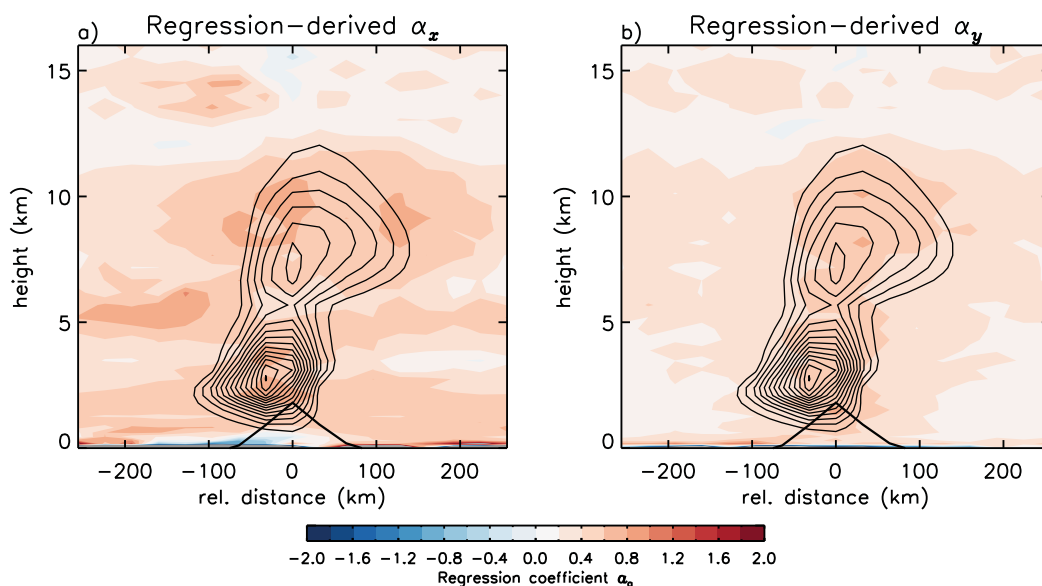


Figure 6. Similar to Figure 5c but where the shading now denotes the regression-derived coefficients, (a) α_x and (b) α_y , obtained in the ESMT version of the SP-WRF. See text for details.

More substantial weakening of the disturbance due to cumulus friction is found in runs where the orientation of the CRM domain is assumed to be perpendicular, rather than parallel to the bulk low-level wind vector of the LSM (results not shown). This increased damping is most likely due to a systematic reduction in the degree of tilting of convective updrafts through its effects on the eddy transport of horizontal momentum [cf. Moncrieff, 1992]. The original (flow-parallel) choice of CRM orientation is therefore near optimal from the standpoint of simulating mesoscale squall lines.

4.2. Tropical Cyclone Case

The setup and forcing for the tropical cyclone (TC) case is identical to the squall line case, except for the following four modifications. First, the horizontal dimensions of the LSM grid are increased from 16×16 to 32×32 columns, to capture a broader range of horizontal wavelengths (up to 1024 km). Second, the target easterly jet profile is replaced by a simpler (nonjet) profile, given by uniform easterlies of 5 m s^{-1} in the lowest 1.5 km, decaying linearly to zero at a height of 13 km (see Figure 7a). Third, the assumption of no ambient rotation on the LSM grid is replaced by a special kind of f -plane condition, whereby the Coriolis force is assumed to act only on perturbation winds about the horizontal domain average; the goal is to prevent the development of domain-averaged horizontal flows, other than those generated through nudging. The value of the Coriolis parameter f is set to $5 \times 10^{-5} \text{ s}^{-1}$, representative of conditions at around 20°N . Fourth, the initial large-scale temperature perturbation used to kick off convection is replaced by an axisymmetric vortex in both hydrostatic and gradient wind balance. As shown in Figure 7b, the vortex has a peak tangential velocity of 10 m s^{-1} , located at a radius of 125 km and a height of 3 km. Wind speeds decay with height above and below this level so that the vortex is confined to the troposphere with a peak surface wind speed of 5 m s^{-1} , i.e., well below tropical storm strength. Finally, because the problem of TC genesis under large-scale vertical shear is highly sensitive to small-scale details in the initial conditions [Zhang and Tao, 2012], an ensemble of 10 simulations is performed. The individual members of the ensemble are made to differ by adding different sets of random temperature perturbations to the initial conditions.

With the exception of the noPGF runs, all simulations feature the development of a TC with maximum 10 m wind speeds V_{max} (relative to the mean flow) in excess of 30 m s^{-1} . Importantly, however, Figure 8 shows that storms in both the ESMT and benchmark ensembles tend to develop roughly 2 days later than in the control ensemble. This later development, together with the slightly weaker end-stage intensity of storms in the ESMT ensemble (as compared to the control ensemble), is evidence once again that the net effect of the explicit momentum feedback is to provide a source of cumulus friction. Also, because no storms

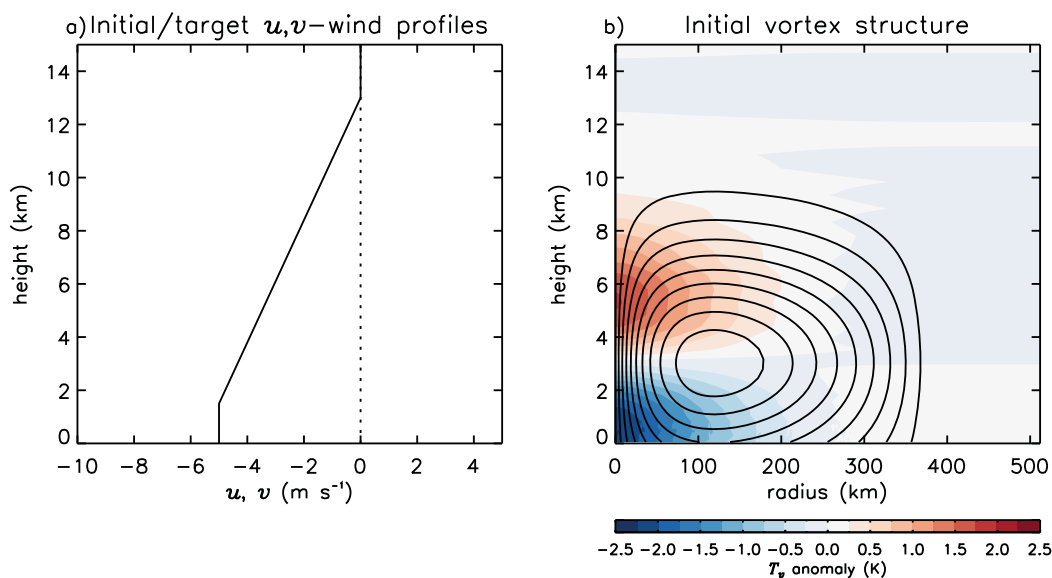


Figure 7. (a) Initial/target u and v -wind profiles and (b) radius-height structure of the initial balanced vortex used in the ensemble of idealized tropical storm runs. Shading in Figure 7b denotes the virtual temperature anomalies with respect to the horizontal domain averaged; contours denote the tangential wind speed at intervals of 1 m s^{-1} .

develop in the set of noPGF runs (results not shown), it appears, as before, that the net effect of the parameterized pressure gradient force is to offset a portion of the cumulus friction. Very similar sorts of findings have been obtained in studies of TC forecast skill using operational models with conventional parameterizations schemes [e.g., Han and Pan, 2006; Hogan and Pauley, 2007].

Considering the horizontal structures of the simulated TCs, Figure 9a shows that storms in the benchmark ensemble tend to have an eye-wall diameter of around 40 km, too small to be captured by the 32 km SP-WRF. This smaller diameter might be expected given the differences in minimum surface pressure shown earlier in Figure 8b. Nevertheless, storms in the ESMT ensemble (Figure 9c) exhibit an azimuthal asymmetry pattern in rainfall that is qualitatively similar to what is seen in the outer portions of the benchmark storms, albeit with exaggerated amplitude. The area-averaged rainfall rates within 150 km of the storm centers are also comparable at roughly 2.5 mm h^{-1} . Storms in the control ensemble (Figure 9b), on the other hand, produce around 15% more area-averaged rain and feature an azimuthal asymmetry pattern that is shifted roughly 45° counterclockwise of the ESMT and benchmark storms.

5. Global Simulations of Seasonal Climate

In order to further evaluate the SP-WRF, a series of seasonal (1 June through 31 August; JJA) global integrations was performed for each of the years 2008–2012. The model is initialized on 29 May using ERA-interim data [Dee et al., 2011] with analysis nudging of horizontal winds, temperature, and water vapor applied during the first 3 days of the simulation (up to 1 June) to allow spin-up of the embedded CRMs. Time-varying SSTs are prescribed using ERA-interim data. The horizontal grid spacing of the LSM is roughly $2.8^\circ \times 2.8^\circ$; the embedded CRMs each have 32 columns at 4 km grid spacing. The vertical grid has 51 levels stretching from a nominal spacing of 50 m near the surface to around 700 m near the model top ($p_{ht} \approx 15 \text{ hPa}$). The large and small-scale time steps are 10 min and 20 s, respectively. The model is evaluated using several different observational data sets that are described in the figure captions.

The above simulation strategy was guided by a recognition that most systematic errors in “warm-start” global climate integrations tend to develop within the first few days of the simulation [Phillips et al., 2004; Klein et al., 2006; Martin et al., 2010; Ma et al., 2013]. Ensembles of relatively short-term (seasonal) integrations can therefore provide a cost-effective means for assessing climate model performance. Here the focus is on the Boreal summer season because previous studies have shown that both the SP-CAM3 and NASA-MMF tend to produce extreme positive biases in rainfall and moisture during this season over the tropical

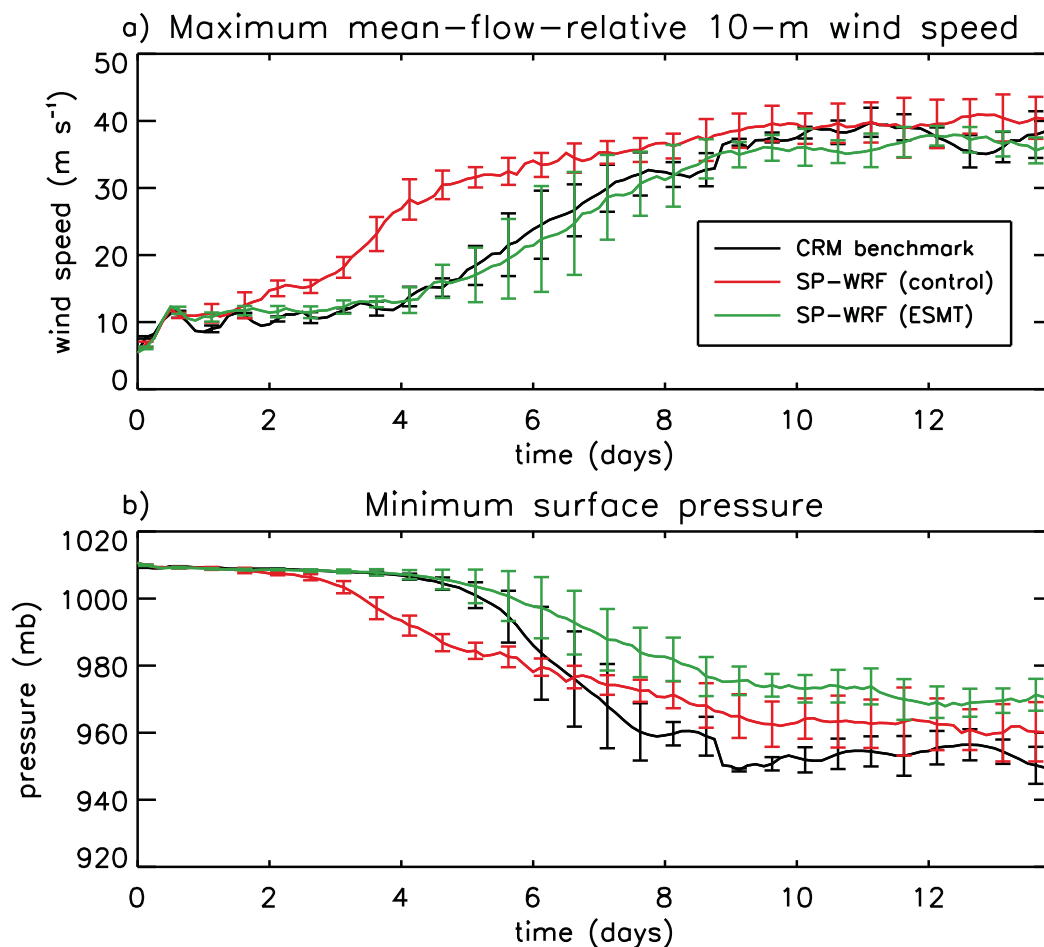


Figure 8. Ensemble-averaged time series of the (a) domain-maximum 10 m wind speed (relative to the domain-average flow) and (b) domain-minimum surface pressure for the simulated tropical storms in the CRM benchmark (black) versus the control (red) and ESMT (green) versions of the SP-WRF. Vertical lines denote the standard deviation among the 10-member ensemble.

northwest Pacific, as part of a hyperactive south Asian summer monsoon [Khairoutdinov *et al.*, 2005; Tao *et al.*, 2009]. This bias pattern is so extreme that it has been given a name, the “Great Red Spot,” based on its stark appearance in color plots of relevant quantities [Randall *et al.*, 2015]. An obvious question then is whether the SP-WRF is plagued by a similar sort of bias?

5.1. Evaluation of the Control Ensemble

5.1.1. Depiction of Time-Mean Fields

Comparison of the top two plots in Figure 10 shows that the control version of the model does a reasonable job at capturing the observed geographic distribution of time-mean surface rainfall—the spatial pattern correlation is 0.84. Referring to the rain error map in Figure 11a, however, we see that the amount of simulated rain is generally too large throughout much of the tropics and Southern Hemisphere extratropics. Geographic areas with especially large and wide-spread positive biases include the equatorial central Pacific and Maritime Continent, as well as the western and eastern coasts of India and further inland over the Himalayas. Conversely, large negative biases are prevalent mainly over the tropical northwest Pacific, where the model fails to produce a well-defined monsoon trough. In response to the question posed earlier, it therefore appears that the model is plagued by essentially the opposite sort of bias as found in the SP-CAM3 and NASA MMF, namely, that of a “Great Blue Spot.” While the reason for this difference is not yet clear, further testing has confirmed that the problem in the SP-WRF is resilient to changes in global model resolution: a similar Great Blue Spot is produced even when the horizontal grid spacing of the LSM is decreased by a factor of two (results not shown).

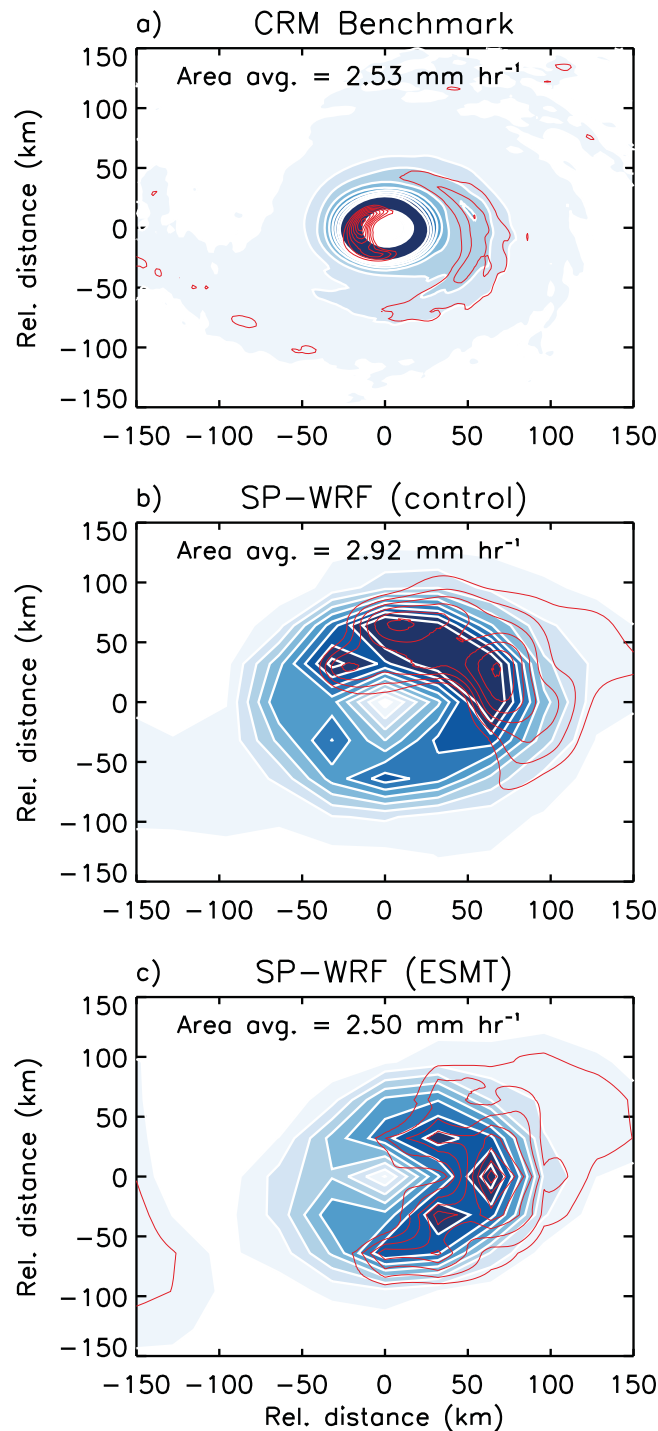


Figure 9. Composite rain structure of the ensemble of tropical storms produced in the (a) CRM benchmark versus the (b) control and (c) ESMT versions of the SP-WRF. Shading plus white contours denote the raw rain rate at intervals of 30 mm h^{-1} , while red contours denote anomalies with respect to the azimuthally averaged rain rate at intervals of 15 mm h^{-1} (only positive values shown). The composites were formed as ensemble and time-averages over the last 5 days of the simulations, with the base point of the composite taken as the locus of minimum surface pressure. The area-averaged rainfall over a circular area within 150 km of the storm center is indicated in each plot.

Taylor diagrams [Taylor, 2001] are used to further evaluate the model's performance. Briefly, these diagrams convey information about the statistical degree of similarity between patterns of simulated versus observed fields. The information is displayed as points on a polar style graph, where the azimuthal position of a point denotes the spatial pattern correlation C , while the radial position denotes the pattern standard deviation of the simulated field normalized by its observed counterpart (i.e., $\hat{\sigma} \equiv \sigma_{sim}/\sigma_{obs}$). Also, the pattern-centered RMSE is given by the distance of a point to the location on the graph where C and $\hat{\sigma}$ are both equal to 1 (i.e., the location corresponding to a perfect match between the model and observations).

Several different fields are considered as part of the model evaluation. These fields include the time-mean global patterns of outgoing longwave radiation (OLR), precipitable water (PW), surface rain rate (R), and u and v -components of the horizontal wind vector at 200 mb and near the surface, denoted [U200, V200] and [U10, V10], respectively. As shown by the red symbols in Figure 12a, the pattern correlation C exceeds 0.75 in all cases, with the simulated OLR showing the best agreement with observations ($C = 0.99$) and the simulated V200 showing the worst agreement ($C = 0.80$). Meanwhile, values of the normalized standard deviation $\hat{\sigma}$ are universally greater than 1, indicating that the model's general circulation and hydrologic cycle are both generally too strong in comparison to observations. These Taylor scores are nevertheless encouraging and were obtained without any effort at "tuning" the model.

Figure 12b is similar to Figure 12a but where the Taylor diagram has been constructed for global patterns of the time-mean zonal anomalies. The correlations in this case are systematically lower (in the range 0.70–0.90), while the normalized pattern standard deviations are generally about the same.

Observed vs simulated time-mean rainfall JJA 2008–2012

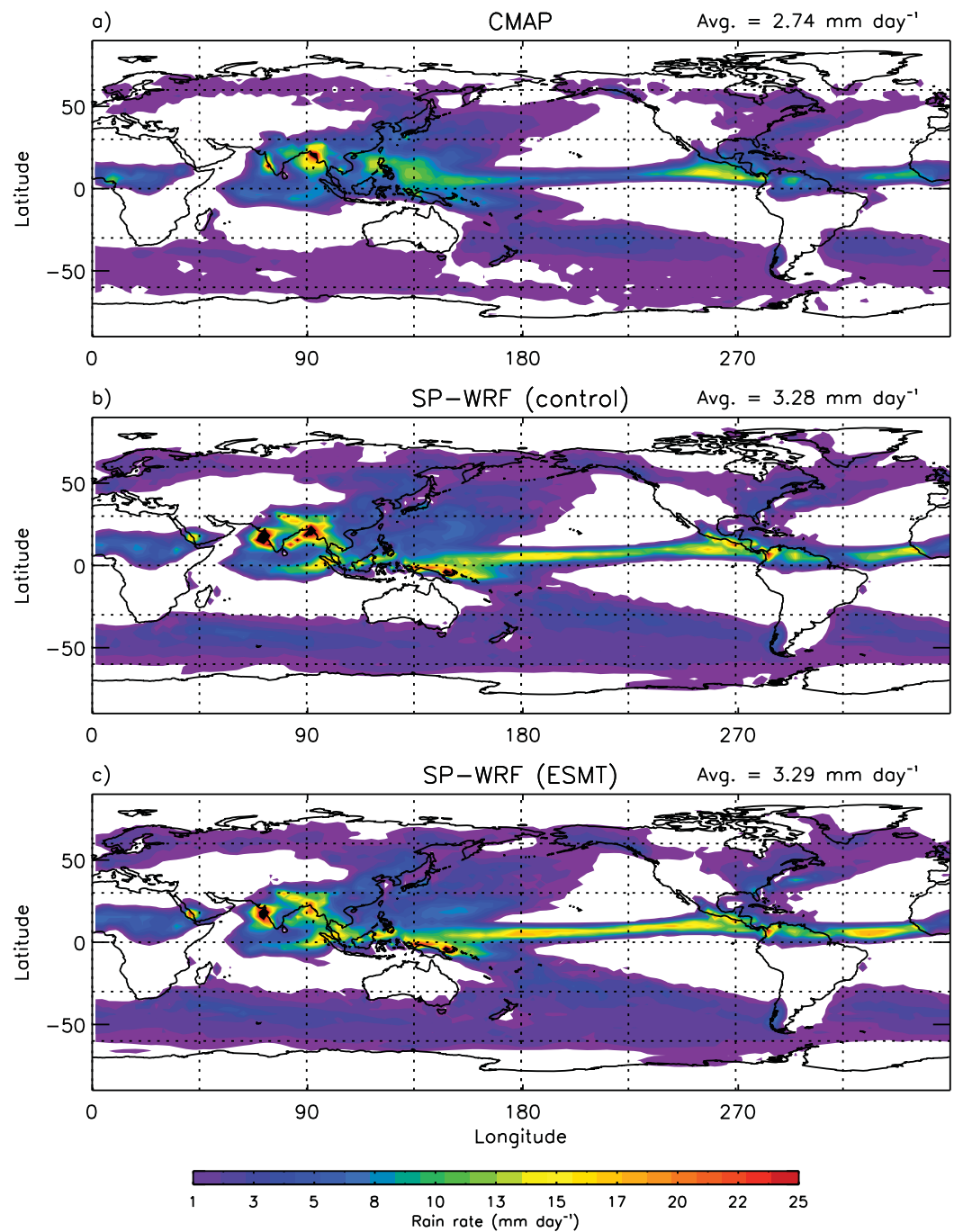


Figure 10. Observed versus simulated time-mean surface rainfall during JJA for the 5 year period 2008–2013. The observed climatology in (a) comes from the Climate Prediction Center’s (CPC’s) Merged Analysis of Precipitation (CMAP), described in *Xie and Arkin [1997]*. Results for the (b) control versus (c) ESMT versions of the SP-WRF are shown.

The one exception is in the case of OLR, where the normalized pattern standard deviation is now well below 1 at $\hat{\sigma} = 0.81$. The interpretation is that zonal fluctuations in the time-mean simulated OLR are generally 20% weaker in amplitude than observed.

To isolate the cause of this deficiency, Figure 13 compares the statistical relationship between the time-mean zonal OLR and rainfall anomalies as seen in the model versus observations. Although the model

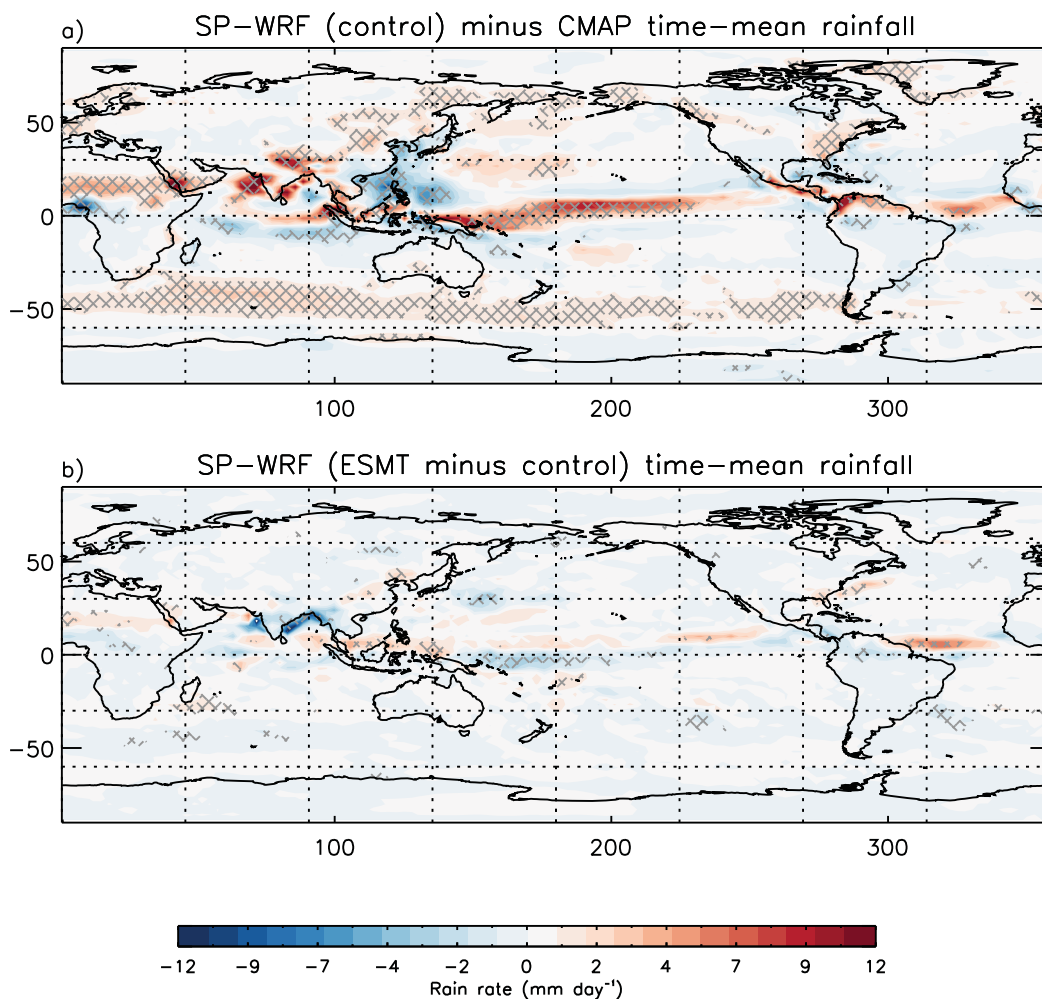


Figure 11. Similar to Figure 10 but for the (a) SP-WRF (control) minus observed rainfall and (b) SP-WRF (ESMT) minus SP-WRF (control) rainfall. The gray hatching in Figure 11a denotes where the absolute difference is statistically significant at the 95% confidence interval or above, based on a two-sided *t* test. The grey hatching in Figure 11b is similar but at the 80% confidence interval.

captures the generally observed decrease in OLR with increasing rainfall (due to increasing upper-level cloudiness with colder emission temperatures), the rate of decrease is about 50% lower, suggesting that the model is not producing enough upper-level cloudiness in precipitating regions. The reason for this lack of upper-level cloudiness is not entirely clear, but may be due partly to deficiencies in the microphysics scheme.

5.1.2. Depiction of Moist Tropical Wave Variability

As already mentioned, previous studies have reported that the depiction of tropical wave variability tends to be greatly improved in SP models, as compared to their conventional counterparts [Khairoutdinov *et al.*, 2008; Tao *et al.*, 2009; McCrary *et al.*, 2014]. While this sort of comparison is beyond the scope of the current study, it is still important to assess the simulated space-time spectrum of tropical rainfall, a key measure of global model fidelity [e.g., Lin *et al.*, 2006; Tulich *et al.*, 2011; Hung *et al.*, 2013; Kim and Alexander, 2013]. Here the spectrum is calculated using an approach similar to that of Wheeler and Kiladis [1999], but with a smaller sliding time window of 30 (rather than 96) days, to increase the number of independent spectral estimates (15 for the five-member ensemble of 92 day runs). Questions about the simulation of important intraseasonal modes of variability, such as the MJO, are therefore left as a topic for future research. To isolate the signals of coherent *submonthly* modes of variability, the resulting raw spectrum is divided by a smoothed “red-noise” background, where the latter is obtained following the approach of Tulich and Kiladis [2012].

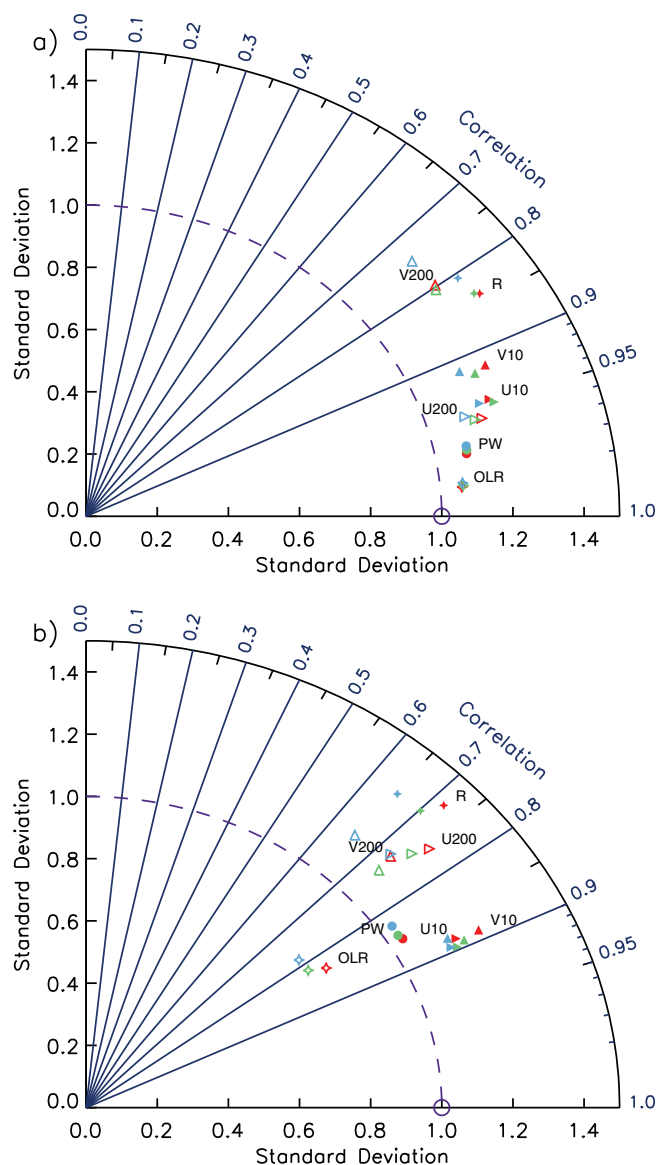


Figure 12. Taylor diagrams for three different versions of the SP-WRF: (1) control (red symbols), (2) ESMT (green symbols), and (3) noPGF (blue symbols). Results in (a) are for time-mean fields in the 5 year ensemble of seasonal (JJA) runs, while those in (b) are for the time-mean zonal anomalies. The observational data sets used to construct these diagrams are as follows. PW: Remote Sensing Systems' (RSS) Total Columnar Water Vapor Product Version-7 (ocean only) [Wentz et al., 2007]; OLR: Clouds and Earth's Radiant Energy Systems (CERES) Energy Balanced and Filled (EBAF) Edition 2.8 [Loeb et al., 2007]; R: CMAP [Xie and Arkin, 1997]; U200, V200, U10, V10: ERA-interim [Dee et al., 2011].

The observed spectrum in Figure 14a shows the familiar signals of relatively fast-moving Kelvin and inertia-gravity (IG) waves with phase speeds in the range 15–30 m s⁻¹, as well as slower-moving easterly waves and tropical depression (TD)-type disturbances with (westward-only) phase speeds in the range 5–10 m s⁻¹. As shown previously by Tulich and Kiladis [2012], the pronounced bias toward westward versus eastward-propagating IG waves can be attributed primarily to interactions between the waves and the background vertical shear in the lower troposphere. The rain spectrum for the control ensemble (Figure 14b) shows all of these observed features. However, the signals of the Kelvin and IG waves are not nearly as pronounced, while the opposite is true of the simulated easterly waves. Also, the implied propagation speed of the IG waves is somewhat slower than observed, so that the distinction between the westward-moving IG and easterly waves is not as clear.

5.2. Effects of Including ESMT

Inclusion of the ESMT formulation is found to improve several aspects of the model performance. Comparison of Figures 10b and 10c (see also Figure 11b) shows that the simulated rain biases are generally smaller over the Indian monsoon region, while comparison of the green versus red symbols in Figure 12 shows that all four of the kinematic fields, U10, V10, U200, and V200, are generally in slightly better agreement with observations, especially when considering fluctuations about the zonal mean (bottom plot). The latter improvements stem mainly from reductions in the normalized pattern standard deviation $\hat{\sigma}$, as opposed to increases in the pattern correlation C . Thus, it appears once again that the net effect of the parameterized CMT is to reduce the overall strength of the simulated circulation, via cumulus friction. Despite these modest improvements, however, some degradation of the simulated rain climatology is apparent over the tropical Atlantic and eastern Pacific, where the overproduction of ITCZ rainfall is exacerbated. This degradation is reflected in Figure 12b by a slight decrease in the pattern correlation C between the simulated versus observed zonal rainfall anomalies.

A more drastic reduction in the rain pattern correlation is found in the noPGF run, as illustrated by the blue symbols in Figure 12. Inclusion of the diagnostic pressure gradient force is therefore acting to prevent the growth of errors in the convection field that would otherwise develop due to overly strong cumulus friction.

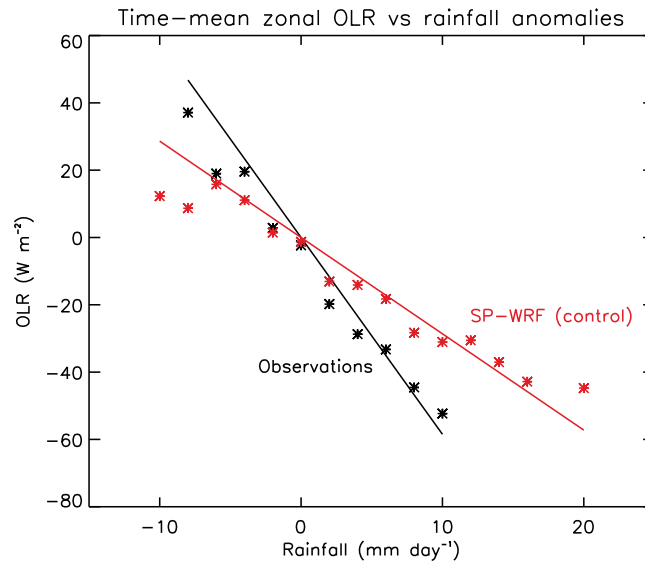


Figure 13. Statistical relationship between time-mean zonal anomalies of OLR versus rainfall as seen in observations (black) and the control version of the SP-WRF (red). Results are plotted as bin-averaged values (symbols), together with a least squares linear fit to the data (lines). The observations are based on the CMAP and CERES products.

Large reductions in C are also apparent for V200, while the remaining kinematic fields exhibit a general decrease in $\hat{\sigma}$, consistent with expected effects of increased cumulus friction. These results are somewhat different from those of Richter and Rasch [2008], who looked at the effects of incorporating traditional mass-flux formulations of CMT in the standard CAM. In particular, they reported the biggest gains in model performance in runs where the effects of the horizontal pressure gradient force were completely neglected (analogous to the noPGF formulation considered here). This difference is presumably due to differences in the underlying pattern of model biases.

Inclusion of the ESMT formulation is also found to improve the depiction of tropical wave variability. The spectrum in Figure 14c shows slightly stronger Kelvin and eastward-moving IG wave signals, as compared to the control spectrum in Figure 14b. The easterly wave signals are also much weaker and more clearly separated from the westward-moving IG waves. The implied propagation speed of the latter wave type is also more in line with observations, although the simulated waves are still too slow.

5.3. Sensitivity of Tropical Rain Biases to CRM Orientation

The choice of CRM orientation is essentially a free parameter in the 2-D SP framework. Here, following the suggestion of Grabowski [2004], the standard approach has been to assume the CRMs are aligned parallel to the averaged large-scale wind vector in the lowest 4 km, denoted $\hat{\mathbf{U}}_{4\text{km}}$. While suitable for deep convective regions under shear, however, this approach is perhaps not as well suited for shallow convective regions under shear, where linear cloud structures, known as “cloud streets,” are common and are typically oriented *parallel*, rather than *perpendicular*, to the mean boundary layer wind vector [Young et al., 2002]. Owing to the use of a 2-D CRM, there is also the related concern of potentially exaggerating the role of low-level shear in generating turbulence and vertical mixing on the CRM grid, which could ultimately affect other aspects of the model performance.

In light of these observations and concerns, a revised strategy has also been tested, in which the CRMs are only aligned parallel to $\hat{\mathbf{U}}_{4\text{km}}$ in cases of strong convection, while being oriented perpendicular otherwise. The criterion used to identify CRMs with strong convection is simply that the domain maximum of $|w_c^*|$ exceed 1 m s^{-1} , where the asterisk denotes that only grid points with a condensed ice/water mixing ratio greater than 0.1 g kg^{-1} are considered. In practice, only a small subset of the CRMs is found to meet the latter criterion ($<15\%$ in the deep tropics 15°S – 15°N). The approach can therefore be considered as generally orthogonal to that of Grabowski [2004]. However, because the CRM orientation is essentially unchanged in regions with predominantly deep convection, any resultant changes in model performance (described below) must ultimately be due to changes in the simulated character and transport properties of boundary layer eddies in predominantly shallow convective regions.

Figure 15 shows that the time-mean pattern of simulated tropical rainfall is generally improved under the revised orientation strategy. Most notably, the spurious enhancements in ITCZ rainfall near the dateline, as well as off the northwestern coast of Sumatra, have both largely been eliminated. The reduction west of Sumatra is spoiled, however, by a broader northward shift in rainfall that results in even larger positive rain biases around the coast of India. These broad-scale changes in rain are obtained regardless of the treatment of CMT. Nevertheless, the improvement over the central Pacific is more pronounced in the run with ESMT.

Observed vs simulated rain spectrum (15S–15N)

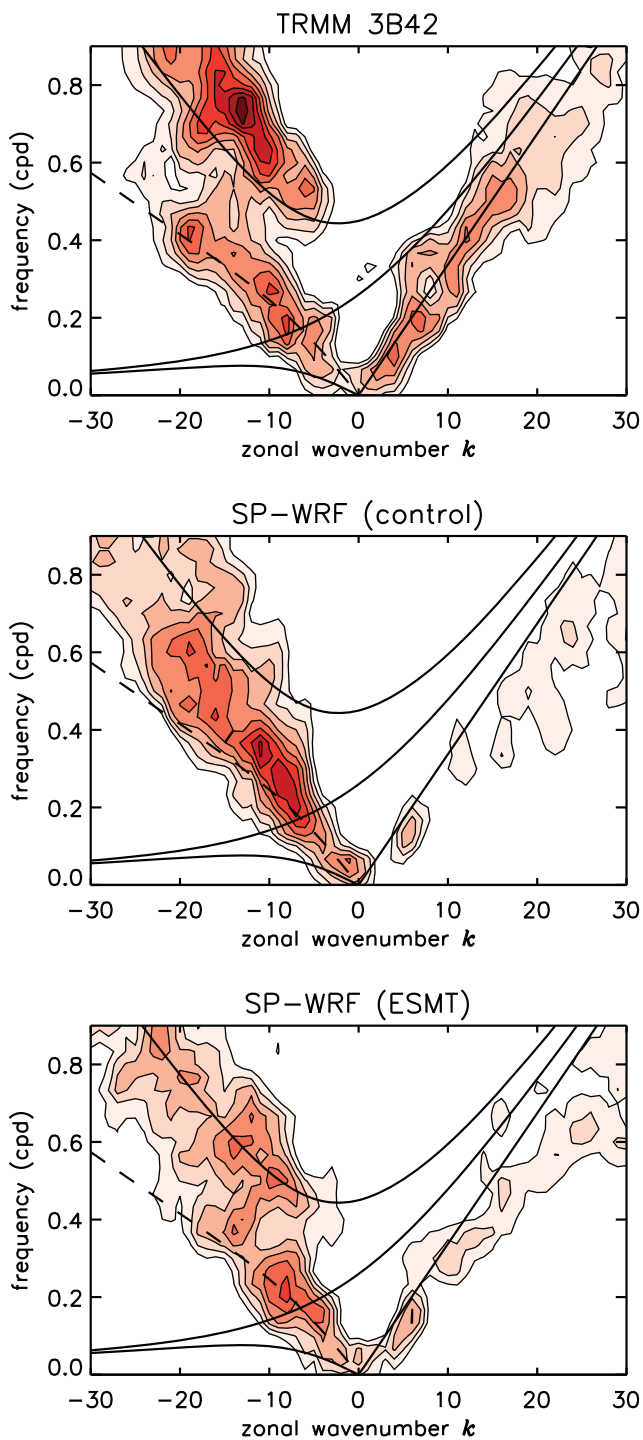


Figure 14. Averaged zonal wavenumber-frequency spectrum of tropical rainfall for latitudes between 15°S and 15°N, as seen in (a) the TRMM 3B42 satellite product [Huffman *et al.*, 2007] versus the (b) control and (c) ESMT versions of the SP-WRF. Solid curves denote the theoretical dispersion properties of dry Kelvin, equatorial Rossby, mixed-Rossby gravity, and the $n = 1$ inertia-gravity modes with an equivalent depth of 25 m. The dashed curve is similar but for the 25 m equatorial Rossby wave under doppler shifting by a uniform easterly flow of 8 m s^{-1} .

The latter simulation also features an improved depiction of ITCZ rainfall over the far western and eastern Pacific, as well as over the tropical north Atlantic, where rainfall is now largest just off the western coast of Africa, similar to observations. However, the amount of simulated rain is still much too high.

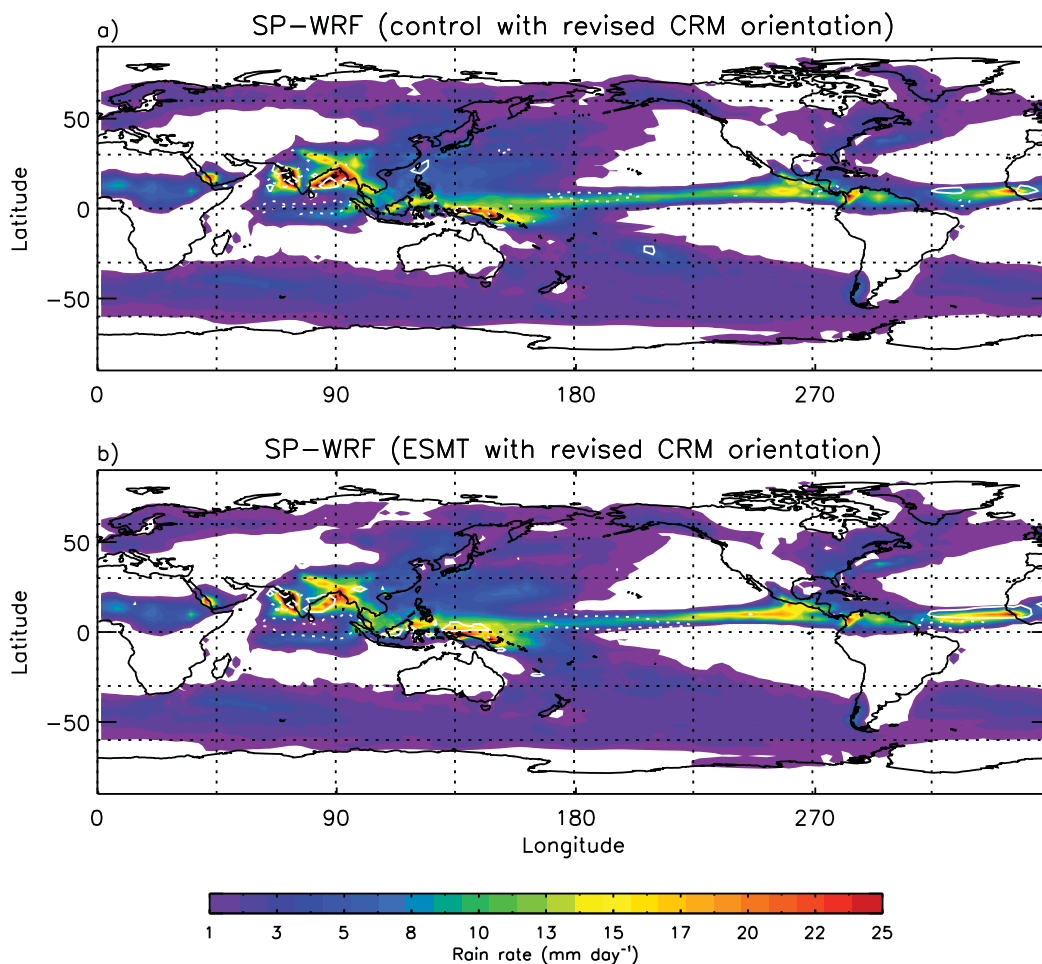


Figure 15. Similar to Figure 10 but for the (a) control and (b) ESMT versions of the SP-WRF with a revised CRM orientation strategy (see text for details). White solid (dotted) contours denote regions where the rainfall difference between the revised-minus-standard-orientation rainfall is >3 (<-3) mm d⁻¹; only differences that are statistically significant at the 80% confidence interval are indicated.

6. Summary and Concluding Remarks

This study developed a unique 2-D SP formulation of the WRF model that, unlike most other formulations, includes the effects of convective momentum transport (CMT) on the large-scale flow. The idea is to treat the two components of the large-scale horizontal momentum as nonconserved scalars that are advected and diffused by the CRM-simulated flow in the presence of a diagnostic source/sink term. The latter is obtained using a linearized version of the Poisson pressure equation, solved at each CRM time step. The approach, referred to as “explicit scalar momentum transport” (ESMT), is therefore similar in concept to traditional mass-flux formulations of CMT. Unlike the latter, however, no assumptions are made concerning the role of the cloud-scale pressure gradient force in producing up or down-gradient CMT.

Despite this generality, results showed that the net effect of the proposed formulation is to produce large-scale cumulus friction, even in simulations of long-lived mesoscale squall lines. In global simulations of seasonal (JJA) climate, it was found that including this additional source of friction led to an improved depiction of coherent synoptic modes of tropical wave variability, in addition to mitigating large positive biases in summer monsoon rainfall along the eastern and western coasts of India. However, this regional bias mitigation was offset by an amplification of rain biases over other tropical regions, including the Atlantic and eastern Pacific. More systematic improvements in the simulated time-mean rain pattern were obtained under a revised CRM-orientation strategy, apparently due to changes in the explicit representation of predominantly shallow convective regions. Neglecting the effects of the horizontal pressure gradient force on CMT was found to have substantial negative impact on model performance.

Results of this study are in broad agreement with those obtained in previous climate simulation studies performed using the SP-CAM3. In particular, studies by *Khairoutdinov et al.* [2005] and *Khairoutdinov et al.* [2008] have shown how biases in the SP-CAM3's depiction of time-mean rainfall can be mitigated by either: (1) changing the orientation of the embedded 2-D CRMs from being everywhere in the east-west to north-south direction or (2) explicitly including the effects of CMT by replacing the host model's 2-D CRMs with a set of 3-D CRMs (while keeping the total number of CRM grid columns the same). Similar sorts of findings were later reported by *Cheng and Xu* [2014], using a modified version of the SP-CAM3, similar in some respects to the SP-WRF introduced here. What has perhaps not been appreciated in these studies, however, is that much of the SP-CAM3's sensitivity to the choice of CRM orientation may in fact be due to changes in the simulated character of shallow convective clouds and turbulence, as opposed to changes in the simulated character of deep convective clouds, as might naively be expected. Further research is therefore needed to clarify how the choice of CRM orientation influences the explicit simulation of *all* types of convective regimes, including the fair-weather regime of wide-spread shallow convection.

An important contribution of this study is the first-ever benchmark evaluation of the SP approach in the context of TC genesis under shear. A difficulty encountered was that the radial size of the benchmark storm was too small to be adequately resolved by the 32 km horizontal mesh of the SP-WRF. Nevertheless, after coarse graining, the evolution of the maximum surface wind speed in the benchmark storm was seen to be remarkably well captured by the SP model, especially when the effects of CMT were included. This close agreement suggests that the SP approach could ultimately prove useful in applications aimed at predicting and understanding TC-climate linkages, as an extension of previous conventional modeling work by *Held and Zhao* [2011] and many others.

The SP-WRF is a versatile multiscale modeling framework that represents one of only a handful of its kind in the world. Even among these, however, the model is unique in that it can be run in either global or regional configurations with realistic lower boundary conditions and the option of a variety of different bulk physics packages. Also, because the large and small-scale components of the SP-WRF are the same, it is straightforward to precisely evaluate the model against a stand-alone CRM benchmark, as was demonstrated here. Looking forward, it is hoped that these unique capabilities will prove useful not only toward establishing best practices in superparameterized modeling, but also in developing and refining bulk parameterizations for use in global CRMs of the future.

Acknowledgments

The initial seeds of this work were supported by the Water System Program of the National Center for Atmospheric Research, which is funded by the National Science Foundation (NSF). A large majority of the funding and computing resources were provided by the Modeling, Analysis, and Predictions Program of the National Oceanic and Atmospheric (NOAA) Office for Atmospheric and Oceanic Research, with additional funding provided by the NSF AGS grant 1146133. Instructive conversations with David Randall and Brian Mapes were instrumental in arriving at the ESMT formulation. This paper was greatly improved through insightful review comments provided by Mike Pritchard, Robert Pincus, and one anonymous reviewer. The model data described herein have been archived on the NOAA High-Performance Storage System, which can be accessed by registered NOAA affiliates. For unregistered parties, these data can be obtained freely by contacting the author (e-mail: stefan.tulich@noaa.gov).

References

- Andersen, J. A., and Z. Kuang (2011), Moist static energy budget of MJO-like disturbances in the atmosphere of a zonally symmetric aquaplanet, *J. Clim.*, *25*(8), 2782–2804, doi:10.1175/JCLI-D-11-00168.1.
- Arakawa, A., and W. H. Schubert (1974), Interaction of a cumulus cloud ensemble with the large-scale environment, Part I, *J. Atmos. Sci.*, *31*(3), 674–701, doi:10.1175/1520-0469(1974)031<0674:IOACCE>2.0.CO;2.
- Arnold, N. P., Z. Kuang, and E. Tziperman (2013), Enhanced MJO-like variability at high SST, *J. Clim.*, *26*(3), 988–1001, doi:10.1175/JCLI-D-12-00272.1.
- Barnes, G. M., and K. Sieckman (1984), The environment of fast- and slow-moving tropical mesoscale convective cloud lines, *Mon. Weather Rev.*, *112*(9), 1782–1794.
- Benedict, J. J., and D. A. Randall (2011), Impacts of idealized air–sea coupling on Madden-Julian Oscillation structure in the superparameterized CAM, *J. Atmos. Sci.*, *68*(9), 1990–2008, doi:10.1175/JAS-D-11-04.1.
- Cetrone, J., and R. A. Houze (2011), Leading and trailing anvil clouds of west African squall lines, *J. Atmos. Sci.*, *68*, 1114–1123.
- Chen, F., and J. Dudhia (2001), Coupling an advanced land surface–hydrology model with the Penn State–NCAR MM5 modeling system. Part I: Model implementation and sensitivity, *Mon. Weather Rev.*, *129*(4), 569–585, doi:10.1175/1520-0493(2001)129<0569:CAALSH>2.0.CO;2.
- Cheng, A., and K.-M. Xu (2014), An explicit representation of vertical momentum transport in a multiscale modeling framework through its 2D cloud-resolving model component, *J. Geophys. Res. Atmos.*, *119*, 2356–2374, doi:10.1002/2013JD021078.
- Chou, M.-D., and M. J. Suarez (1999), A solar radiation parameterization for atmospheric studies, *Tech. Rep. NASA/TM-1999-104606*, NASA Goddard Space Flight Center, Greenbelt, Md.
- Chou, M.-D., M. J. Suarez, X. Z. Liang, and M.-H. Yan (2001), A thermal infrared radiation parameterization for atmospheric studies, *Tech. Rep. NASA/TM-2001-104606*, NASA Goddard Space Flight Center, Greenbelt, Md.
- Deardorff, J. (1980), Stratocumulus-capped mixed layers derived from a three-dimensional model, *Boundary Layer Meteorol.*, *18*(4), 495–527, doi:10.1007/BF00119502.
- Dee, D. P., et al. (2011), The era-interim reanalysis: Configuration and performance of the data assimilation system, *Q. J. R. Meteorol. Soc.*, *137*(656), 553–597, doi:10.1002/qj.828.
- DeMott, C. A., C. Stan, D. A. Randall, J. L. Kinter, and M. Khairoutdinov (2011), The Asian monsoon in the superparameterized CCSM and its relationship to tropical wave activity, *J. Clim.*, *24*(19), 5134–5156, doi:10.1175/2011JCLI4202.1.
- Fairall, C. W., E. F. Bradley, J. E. Hare, A. A. Grachev, and J. B. Edson (2003), Bulk parameterization of air–sea fluxes: Updates and verification for the COARE algorithm, *J. Clim.*, *16*(4), 571–591, doi:10.1175/1520-0442(2003)016<0571:BPOASF>2.0.CO;2.
- Grabowski, W. W. (2001), Coupling cloud processes with the large-scale dynamics using the Cloud-Resolving Convection Parameterization (CRCP), *J. Atmos. Sci.*, *58*(9), 978–997, doi:10.1175/1520-0469(2001)058<0978:CCPWTL>2.0.CO;2.

- Grabowski, W. W. (2003), MJO-like coherent structures: Sensitivity simulations using the Cloud-Resolving Convection Parameterization (CRCP), *J. Atmos. Sci.*, *60*(6), 847–864, doi:10.1175/1520-0469(2003)060<0847:MLCSSS>2.0.CO;2.
- Grabowski, W. W. (2004), An improved framework for superparameterization, *J. Atmos. Sci.*, *61*(15), 1940–1952, doi:10.1175/1520-0469(2004)061<1940:AIFFS>2.0.CO;2.
- Grabowski, W. W. (2006), Impact of explicit atmosphere–ocean coupling on MJO-like coherent structures in idealized aquaplanet simulations, *J. Atmos. Sci.*, *63*(9), 2289–2306, doi:10.1175/JAS3740.1.
- Grabowski, W. W., and P. K. Smolarkiewicz (1999), CRCP: A Cloud Resolving Convection Parameterization for modeling the tropical convecting atmosphere, *Physica D*, *133*(1–4), 171–178, doi:10.1016/S0167-2789(99)00104-9.
- Gregory, D., R. Kershaw, and P. M. Inness (1997), Parametrization of momentum transport by convection. II: Tests in single-column and general circulation models, *Q. J. R. Meteorol. Soc.*, *123*(541), 1153–1183, doi:10.1002/qj.49712354103.
- Han, J., and H.-L. Pan (2006), Sensitivity of hurricane intensity forecast to convective momentum transport parameterization, *Mon. Weather Rev.*, *134*(2), 664–674, doi:10.1175/MWR3090.1.
- Held, I. M., and M. Zhao (2011), The response of tropical cyclone statistics to an increase in CO₂ with fixed sea surface temperatures, *J. Clim.*, *24*(20), 5353–5364, doi:10.1175/JCLI-D-11-00050.1.
- Hogan, T. F., and R. L. Pauley (2007), The impact of convective momentum transport on tropical cyclone track forecasts using the Emanuel cumulus parameterization, *Mon. Weather Rev.*, *135*(4), 1195–1207, doi:10.1175/MWR3365.1.
- Hong, S.-Y., Y. Noh, and J. Dudhia (2006), A new vertical diffusion package with an explicit treatment of entrainment processes, *Mon. Weather Rev.*, *134*, 2318–2341.
- Huffman, G. J., R. F. Adler, D. T. Bolvin, G. Gu, E. J. Nelkin, K. P., Bowman, Y. Hong, E. F. Stocker, and D. B. Wolf (2007), The TRMM Multisatellite Precipitation Analysis (TMPA): Quasi-global, multiyear, combined-sensor precipitation estimates at fine scale, *J. Hydrometeorol.*, *8*, 38–55.
- Hung, M.-P., J.-L. Lin, W. Wang, D. Kim, T. Shinoda, and S. J. Weaver (2013), MJO and convectively coupled equatorial waves simulated by CMIP5 climate models, *J. Clim.*, *26*(17), 6185–6214, doi:10.1175/JCLI-D-12-00541.1.
- Jung, J.-H., and A. Arakawa (2005), Preliminary tests of multiscale modeling with a two-dimensional framework: Sensitivity to coupling methods, *Mon. Weather Rev.*, *133*(3), 649–662, doi:10.1175/MWR-2878.1.
- Jung, J.-H., and A. Arakawa (2014), Modeling the moist-convective atmosphere with a quasi-3-D multiscale modeling framework (Q3D MMF), *J. Adv. Model. Earth Syst.*, *6*, 185–205, doi:10.1002/2013MS000295.
- Khairoutdinov, M., D. Randall, and C. DeMott (2005), Simulations of the atmospheric general circulation using a cloud-resolving model as a superparameterization of physical processes, *J. Atmos. Sci.*, *62*, 2136–2154.
- Khairoutdinov, M., C. DeMott, and D. Randall (2008), Evaluation of the simulated interannual and subseasonal variability in an AMIP-style simulation using the CSU Multiscale Modeling Framework, *J. Clim.*, *21*, 413–431.
- Kim, D., J.-S. Kug, I.-S. Kang, F.-F. Jin, and A. Wittenberg (2008), Tropical pacific impacts of convective momentum transport in the SNU coupled GCM, *Clim. Dyn.*, *31*(2–3), 213–226, doi:10.1007/s00382-007-0348-4.
- Kim, J.-E., and M. J. Alexander (2013), Tropical precipitation variability and convectively coupled equatorial waves on submonthly time scales in reanalyses and TRMM, *J. Clim.*, *26*(10), 3013–3030, doi:10.1175/JCLI-D-12-00353.1.
- Kim, Y.-J., and A. Arakawa (1995), Improvement of orographic gravity wave parameterization using a mesoscale gravity wave model, *J. Atmos. Sci.*, *52*(11), 1875–1902, doi:10.1175/1520-0469(1995)052<1875:IOGWP>2.0.CO;2.
- Klein, S. A., X. Jiang, J. Boyle, S. Malyshev, and S. Xie (2006), Diagnosis of the summertime warm and dry bias over the U.S. southern great plains in the GFDL climate model using a weather forecasting approach, *Geophys. Res. Lett.*, *33*, L18805, doi:10.1029/2006GL027567.
- Klemp, J. B., W. C. Skamarock, and J. Dudhia (2007), Conservative split-explicit time integration methods for the compressible nonhydrostatic equations, *Mon. Weather Rev.*, *135*(8), 2897–2913, doi:10.1175/MWR3440.1.
- Klemp, J. B., J. Dudhia, and A. D. Hassiotis (2008), An upper gravity-wave absorbing layer for nwp applications, *Mon. Weather Rev.*, *136*(10), 3987–4004, doi:10.1175/2008MWR2596.1.
- Lafore, J.-P., J.-L. Redelsperger, and G. Jaubert (1988), Comparison between a three-dimensional simulation and doppler radar data of a tropical squall line: Transports of mass, momentum, heat, and moisture, *J. Atmos. Sci.*, *45*(22), 3483–3500, doi:10.1175/1520-0469(1988)045<3483:CBATDS>2.0.CO;2.
- Lane, T. P., and M. W. Moncrieff (2010), Characterization of momentum transport associated with organized moist convection and gravity waves, *J. Atmos. Sci.*, *67*(10), 3208–3225, doi:10.1175/2010JAS3418.1.
- LeMone, M. A., G. M. Barnes, and E. J. Zipser (1984), Momentum flux by lines of cumulonimbus over the tropical oceans, *J. Atmos. Sci.*, *41*(12), 1914–1932, doi:10.1175/1520-0469(1984)041<1914:MFBLOC>2.0.CO;2.
- Lemone, M. A., L. F. Tarleton, and G. M. Barnes (1988), Perturbation pressure at the base of cumulus clouds in low shear, *Mon. Weather Rev.*, *116*(10), 2062–2068, doi:10.1175/1520-0493(1988)116<2062:PPATBO>2.0.CO;2.
- LeMone, M. A., E. J. Zipser, and S. B. Trier (1998), The role of environmental shear and thermodynamic conditions in determining the structure and evolution of mesoscale convective systems during toga coare, *J. Atmos. Sci.*, *55*(23), 3493–3518, doi:10.1175/1520-0469(1998)055<3493:TROESA>2.0.CO;2.
- Lin, J.-L., et al. (2006), Tropical intraseasonal variability in 14 IPCC AR4 climate models. Part I: Convective signals, *J. Clim.*, *19*, 2665–2690.
- Loeb, N. G., S. Kato, K. Loukachine, N. Manalo-Smith, and D. R. Doelling (2007), Angular distribution models for top-of-atmosphere radiative flux estimation from the clouds and the earth’s radiant energy system instrument on the terra satellite. Part ii: Validation, *J. Atmos. Oceanic Technol.*, *24*(4), 564–584, doi:10.1175/JTECH1983.1.
- Ma, H. Y., et al. (2013), On the correspondence between mean forecast errors and climate errors in CMIP5 models, *J. Clim.*, *27*(4), 1781–1798, doi:10.1175/JCLI-D-13-00474.1.
- Mapes, B. E., and X. Wu (2001), Notes and correspondence convective eddy momentum tendencies in long cloud-resolving model simulations, *J. Atmos. Sci.*, *58*(5), 517–526, doi:10.1175/1520-0469(2001)058<0517:NACCEM>2.0.CO;2.
- Martin, G. M., S. F. Milton, C. A. Senior, M. E. Brooks, S. Ineson, T. Reichler, and J. Kim (2010), Analysis and reduction of systematic errors through a seamless approach to modeling weather and climate, *J. Clim.*, *23*(22), 5933–5957, doi:10.1175/2010JCLI3541.1.
- McCrary, R. R., D. A. Randall, and C. Stan (2014), Simulations of the west African monsoon with a superparameterized climate model. Part II: African easterly waves, *J. Clim.*, *27*(22), 8323–8341, doi:10.1175/JCLI-D-13-00677.1.
- Mizuta, R., K. Oouchi, H. Yoshimura, A. Noda, K. Katayama, S. Yukimoto, M. Hosaka, S. Kusunoki, H. Kawai, and M. Nakagawa (2006), 20-km-mesh global climate simulations using JMA-GSM model—Mean climate states, *J. Meteorol. Soc. Jpn.*, *84*(1), 165–185.
- Moncrieff, M. W. (1992), Organized convective systems: Archetypal dynamical models, mass and momentum flux theory, and parameterization, *Q. J. R. Meteorol. Soc.*, *118*(507), 819–850, doi:10.1002/qj.49711850703.

- Pauluis, O., and S. Garner (2006), Sensitivity of radiative–convective equilibrium simulations to horizontal resolution, *J. Atmos. Sci.*, *63*(7), 1910–1923, doi:10.1175/JAS3705.1.
- Phillips, T. J., G. L. Potter, D. L. Williamson, R. T. Cederwall, J. S. Boyle, M. Fiorino, J. J. Hnilo, J. G. Olson, S. Xie, and J. J. Yio (2004), Evaluating parameterizations in general circulation models: Climate simulation meets weather prediction, *Bull. Am. Meteorol. Soc.*, *85*(12), 1903–1915, doi:10.1175/BAMS-85-12-1903.
- Pope, V. D., M. L. Gallani, P. R. Rowntree, and R. A. Stratton (2000), The impact of new physical parametrizations in the Hadley Centre climate model: HadAM3, *Clim. Dyn.*, *16*(2–3), 123–146, doi:10.1007/s003820050009.
- Pritchard, M. S., and C. S. Bretherton (2014), Causal evidence that rotational moisture advection is critical to the superparameterized Madden–Julian oscillation, *J. Atmos. Sci.*, *71*(2), 800–815, doi:10.1175/JAS-D-13-0119.1.
- Pritchard, M. S., M. W. Moncrieff, and R. C. J. Somerville (2011), Orographic propagating precipitation systems over the United States in a global climate model with embedded explicit convection, *J. Atmos. Sci.*, *68*(8), 1821–1840, doi:10.1175/2011JAS3699.1.
- Randall, D., M. Khairoutdinov, A. Arakawa, and W. Grabowski (2003), Breaking the cloud parameterization deadlock, *Bull. Am. Meteorol. Soc.*, *84*(11), 1547–1564, doi:10.1175/BAMS-84-11-1547.
- Randall, D., D. C. C. Stan, M. Khairoutdinov, J. Benedict, R. McCrary, and K. Thayer-Calder (2015), Simulations of the tropical general circulation with a multiscale global model, in *Multiscale Convection-Coupled Systems in the Tropics*, Meteorol. Monogr., edited by R. Fovell and W.-W. Tung, Am. Meteorol. Soc., in press.
- Richter, J. H., and P. J. Rasch (2008), Effects of convective momentum transport on the atmospheric circulation in the Community Atmosphere Model, Version 3, *J. Clim.*, *21*(7), 1487–1499, doi:10.1175/2007JCLI1789.1.
- Rickenbach, T., R. Nieto Ferreira, N. Guy, and E. Williams (2009), Radar-observed squall line propagation and the diurnal cycle of convection in Niamey, Niger, during the 2006 African monsoon and multidisciplinary analyses intensive observing period, *J. Geophys. Res.*, *114*, D03107, doi:10.1029/2008JD01087.
- Romps, D. M. (2012), On the equivalence of two schemes for convective momentum transport, *J. Atmos. Sci.*, *69*(12), 3491–3500, doi:10.1175/JAS-D-12-068.1.
- Rotunno, R., and J. B. Klemp (1982), The influence of the shear-induced pressure gradient on thunderstorm motion, *Mon. Weather Rev.*, *110*(2), 136–151, doi:10.1175/1520-0493(1982)110<0136:TIOTS>2.0.CO;2.
- Schneider, E. K., and R. S. Lindzen (1976), A discussion of the parameterization of momentum exchange by cumulus convection, *J. Geophys. Res.*, *81*(18), 3158–3160, doi:10.1029/JC081i018p03158.
- Shapiro, L. J., and D. E. Stevens (1980), Parameterization of convective effects on the momentum and vorticity budgets of synoptic-scale Atlantic tropical waves, *Mon. Weather Rev.*, *108*(11), 1816–1826, doi:10.1175/1520-0493(1980)108<1816:POCEOT>2.0.CO;2.
- Shaw, T. A., and T. P. Lane (2013), Toward an understanding of vertical momentum transports in cloud-system-resolving model simulations of multiscale tropical convection, *J. Atmos. Sci.*, *70*(10), 3231–3247, doi:10.1175/JAS-D-13-068.1.
- Skamarock, W. C., and M. L. Weisman (2009), The impact of positive-definite moisture transport on NWP precipitation forecasts, *Mon. Weather Rev.*, *137*(1), 488–494, doi:10.1175/2008MWR2583.1.
- Skamarock, W. C., J. B. Klemp, J. Dudhia, D. O. Gill, D. M. Barker, W. Wang, and J. G. Powers (2008), A description of the Advanced Research WRF Version 3, NCAR Tech. Note NCAR/TN-475+STR, Mesoscale and Microscale Meteorology Division of the Nat. Cent. Atmos. Res., Boulder, Colo.
- Slawinska, J., O. Pauluis, A. J. Majda, and W. W. Grabowski (2015), Multiscale interactions in an idealized Walker cell: Simulations with sparse space–time superparameterization, *Mon. Weather Rev.*, *143*(2), 563–580, doi:10.1175/MWR-D-14-00082.1.
- Soong, S.-T., and W.-K. Tao (1984), A numerical study of the vertical transport of momentum in a tropical rainband, *J. Atmos. Sci.*, *41*(6), 1049–1061, doi:10.1175/1520-0469(1984)041<1049:ANSOTV>2.0.CO;2.
- Stan, C., M. Khairoutdinov, C. A. DeMott, V. Krishnamurthy, D. M. Straus, D. A. Randall, J. L. Kinter, and J. Shukla (2010), An ocean–atmosphere climate simulation with an embedded cloud resolving model, *Geophys. Res. Lett.*, *37*, L01702, doi:10.1029/2009GL040822.
- Tao, W.-K., et al. (2003), Microphysics, radiation and surface processes in the Goddard Cumulus Ensemble (GCE) model, *Meteorol. Atmos. Phys.*, *82*(1), 97–137.
- Tao, W.-K., et al. (2009), A multiscale modeling system: Developments, applications, and critical issues, *Bull. Am. Meteorol. Soc.*, *90*(4), 515–534, doi:10.1175/2008BAMS2542.1.
- Taylor, K. E. (2001), Summarizing multiple aspects of model performance in a single diagram, *J. Geophys. Res.*, *106*(D7), 7183–7192, doi:10.1029/2000JD900719.
- Thayer-Calder, K., and D. A. Randall (2009), The role of convective moistening in the Madden–Julian oscillation, *J. Atmos. Sci.*, *66*(11), 3297–3312, doi:10.1175/2009JAS3081.1.
- Tulich, S., G. Kiladis, and A. Suzuki-Parker (2011), Convectively coupled Kelvin and easterly waves in a regional climate simulation of the tropics, *Clim. Dyn.*, *36*(1–2), 185–203, doi:10.1007/s00382-009-0697-2.
- Tulich, S. N., and G. N. Kiladis (2012), Squall lines and convectively coupled gravity waves in the tropics: Why do most cloud systems propagate westward?, *J. Atmos. Sci.*, *69*(10), 2995–3012, doi:10.1175/JAS-D-11-0297.1.
- Tulich, S. N., and B. E. Mapes (2010), Transient environmental sensitivities of explicitly simulated tropical convection, *J. Atmos. Sci.*, *67*(4), 923–940.
- Tung, W.-W., and M. Yanai (2002), Convective momentum transport observed during the TOGA COARE IOP. Part I: General features, *J. Atmos. Sci.*, *59*(11), 1857–1871, doi:10.1175/1520-0469(2002)059<1857:CMTODT>2.0.CO;2.
- Wentz, F. J., L. Ricciardulli, K. Hilburn, and C. Mears (2007), How much more rain will global warming bring?, *Science*, *317*(5835), 233–235, doi:10.1126/science.1140746.
- Wheeler, M., and G. N. Kiladis (1999), Convectively coupled equatorial waves: Analysis of clouds and temperature in the wavenumber–frequency domain, *J. Atmos. Sci.*, *56*, 374–399.
- Wicker, L. J., and W. C. Skamarock (2002), Time-splitting methods for elastic models using forward time schemes, *Mon. Weather Rev.*, *130*(8), 2088–2097, doi:10.1175/1520-0493(2002)130<2088:TSMFEM>2.0.CO;2.
- Wu, X., and M. Yanai (1994), Effects of vertical wind shear on the cumulus transport of momentum: Observations and parameterization, *J. Atmos. Sci.*, *51*(12), 1640–1660, doi:10.1175/1520-0469(1994)051<1640:EOVWSO>2.0.CO;2.
- Wyant, M. C., C. S. Bretherton, and P. N. Blossey (2009), Subtropical low cloud response to a warmer climate in a superparameterized climate model. Part I: Regime sorting and physical mechanisms, *J. Adv. Model. Earth Syst.*, *1*, doi:10.3894/JAMES.2009.1.7.
- Xie, P., and P. A. Arkin (1997), Global precipitation: A 17-year monthly analysis based on gauge observations, satellite estimates, and numerical model outputs, *Bull. Am. Meteorol. Soc.*, *78*(11), 2539–2558, doi:10.1175/1520-0477(1997)078<2539:GPAYMA>2.0.CO;2.

- Young, G. S., D. A. R. Kristovich, M. R. Hjelmfelt, and R. C. Foster (2002), Rolls, streets, waves, and more: A review of quasi-two-dimensional structures in the atmospheric boundary layer, *Bull. Am. Meteorol. Soc.*, *83*(7), 997–1001, doi:10.1175/1520-0477(2002)083<0997:RSWA-MA>2.3.CO;2.
- Zeng, X., and A. Beljaars (2005), A prognostic scheme of sea surface skin temperature for modeling and data assimilation, *Geophys. Res. Lett.*, *32*, L14605, doi:10.1029/2005GL023030.
- Zhang, F., and D. Tao (2012), Effects of vertical wind shear on the predictability of tropical cyclones, *J. Atmos. Sci.*, *70*(3), 975–983, doi:10.1175/JAS-D-12-0133.1.
- Zhang, G. J., and H.-R. Cho (1991), Parameterization of the vertical transport of momentum by cumulus clouds. Part I: Theory, *J. Atmos. Sci.*, *48*(12), 1483–1492, doi:10.1175/1520-0469(1991)048<1483:POTVTO>2.0.CO;2.
- Zhang, G. J., and X. Wu (2003), Convective momentum transport and perturbation pressure field from a cloud-resolving model simulation, *J. Atmos. Sci.*, *60*(9), 1120–1139, doi:10.1175/1520-0469(2003)060<1120:CMTAPP>2.0.CO;2.
- Zilitinkevich, S. (1995), *Non-Local Turbulent Transport: Pollution Dispersion Aspects of Coherent Structure of Convective Flows, Air Pollution III, vol. 1, Air Pollution Theory and Simulations*, edited by H. Power, N. Moussiopoulos, and C. A. Brebbia, pp. 53–60, Computational Mechanics Publications, Southampton, U. K.